

The Thermal Evolution of the Donors in AM CVn Binaries

Christopher J. Deloye,^{1*} Ronald E. Taam,¹ Christophe Winisdoerffer,² and Gilles Chabrier²

¹*Department of Physics & Astronomy, Northwestern University, 2131 Tech Drive, Evanston, IL 60208*

²*Ecole normale supérieure de Lyon, CRAL (UMR CNRS No. 5574), 69364 Lyon Cedex 07, France*

27 October 2018

ABSTRACT

We calculate the full stellar-structural evolution of donors in AM CVn systems formed through the WD channel coupled to the binary’s evolution. Contrary to assumptions made in prior modelling, these donors are not fully convective over much of the AM CVn phase and do not evolve adiabatically under mass loss indefinitely. Instead, we identify three distinct phases of evolution: a mass transfer turn-on phase (during which P_{orb} continues to decrease even after contact, the donor contracts, and the mass transfer rate accelerates to its maximum), a phase in which the donor expands adiabatically in response to mass loss, and a cooling phase beginning at $P_{\text{orb}} \approx 45\text{--}55$ minutes during which the donor contracts. The physics that determines the behaviour in the first and third phases, both of which are new outcomes of this study, are discussed in some detail. We find the overall duration of the turn-on phase to be between $\sim 10^4\text{--}10^6$ yrs, significantly longer than prior estimates. We predict the donor’s luminosity, L , and effective temperature, T_{eff} . During the adiabatic expansion phase (ignoring irradiation effects), $L \approx 10^{-6}\text{--}10^{-4}L_{\odot}$ and $T_{\text{eff}} \approx 1000\text{--}1800$ K. However, the flux generated in the accretion flow dominates the donor’s intrinsic light at all times. The impact of irradiation on the donor extends the phase of adiabatic expansion to longer P_{orb} , slows the contraction during the cooling phase, and alters the donor’s observational characteristics. Irradiated donors during the adiabatic phase can attain surface luminosities up to $\approx 10^{-2}L_{\odot}$. We argue that the turn-on and cooling phases both will leave significant imprints on the AM CVn population’s P_{orb} -distribution. Finally, we show that the eclipsing AM CVn system SDSS J0926+3624 provides evidence that WD-channel systems with non-zero entropy donors contribute to the AM CVn population, and we discuss the observational signature of the donor in this system.

Key words: binaries: close—gravitational waves—stars:individual (RX J0806+1527, RX J1914+2456, SDSS J0926+3624)—white dwarfs

1 INTRODUCTION

The AM Canum Venaticorum (AM CVn) variables are a class of He-rich objects with variability periods of $\approx 5\text{--}66$ minutes. Various lines of evidence (see §1 of Deloye et al. 2005, for a brief summary) indicate these periods are orbital in origin and that ongoing mass-transfer from a low-mass, essentially pure-He donor onto a white dwarf (WD) accretor is taking place. Thus, AM CVn systems form the WD-accreting class of so-called ultracompact binaries: interacting stellar binaries with orbital periods, P_{orb} , below the minimum P_{orb} attainable by H-dominated objects ($\approx 70\text{--}80$ minutes, see, e.g., Kolb & Baraffe 1999). At such short P_{orb} , the binary evolution is driven by orbital angular momentum losses due to gravity-wave (GW) emission.

The AM CVn objects represent an extreme end-product

of stellar-binary evolution and at least some of them are examples of WD-WD binaries that survived the transition from a detached phase of GW-driven in-spiral to their current state of stable mass-transfer. There are significant uncertainties concerning aspects of both the prior binary evolution (most importantly the outcome of common-envelope events; Paczynski 1976) and the outcomes of WD-WD binaries initiating mass transfer. The characteristics of the AM CVn population can thus provide insights into the physics important to both these phases of their prior evolution. It is expected that space-based GW interferometers, such as the proposed *LISA* mission¹, will detect essentially the entire galactic population of AM CVns with $P_{\text{orb}} \lesssim 20$ minutes (Nelemans et al. 2001; Deloye et al. 2005), providing an observational picture of unprecedented detail. Future prospects

* E-mail: cjdeloye@northwestern.edu

¹ <http://lisa.nasa.gov/>

for strong constraints from the AM CVn population on our theories of binary formation and evolution are, thus, very bright. In the meantime, advances from electromagnetic observations and developing theory will begin addressing these same questions.

There have been three distinct binary evolution channels proposed to form AM CVn systems. Two of these formation channels involve a series of two common-envelope (CE) events which bring the remnant cores of a main-sequence (MS) binary close enough for GW-emission to drive them into contact, initiating the AM CVn phase. These channels are distinguished by the state of the proto-donor prior to contact (Nelemans et al. 2001). In what we'll call the He-star channel, the proto-donor is able to ignite He prior to contact. In the other, which we'll refer to as the WD channel, the donor is partially-to-very degenerate (Deloye et al. 2005) and has not undergone any He burning. The third channel involves an evolved MS star with a WD companion starting stable mass transfer just before it evolves up the red-giant branch (Podsiadlowski et al. 2003). The star's core is dominated by He, allowing the binary to evolve to ultracompact configurations. We'll refer to this third channel as the evolved-MS channel.

In mass transferring binaries, the donor's structural response to mass loss plays a central role in determining the binary's evolution (see, e.g., Deloye & Bildsten 2003). The extent to which the donors from each formation channel have been modelled varies considerably. He-star channel donors have only been modelled by a fit (Nelemans et al. 2001) to a single relevant binary evolution calculation by Tutukov & Fedorova (1989). The WD channel donors have been considered more extensively. Nelemans et al. (2001) modelled these donors as fully-degenerate WDs obeying the zero-temperature He WD mass-radius (M - R) relation. Later, Deloye et al. (2005), using donor structural models developed for ultracompact low-mass X-ray binaries (Deloye & Bildsten 2003), modelled the evolution of non-zero entropy donors from the WD-channel. Podsiadlowski et al. (2003) has presented a detailed study of the evolved-MS star channel.

In this paper, we focus on the WD channel systems. The Deloye et al. (2005) study had several limitations: they assumed the donors to be fully convective and to evolve adiabatically under mass loss due to the very large mass transfer rates, \dot{M} , produced in AM CVns. With these assumptions, the evolution is completely determined by the total mass of the two components and the donor's specific entropy, which determines the M - R relation the donor follows and, amongst other system parameters, the binary's $\dot{M}(P_{\text{orb}})$ evolution. The inclusion of non-zero entropy donors in this population resulted in shifting systems to larger \dot{M} at fixed P_{orb} and allowed systems to evolve out to longer P_{orb} as compared to a population of zero-temperature donors. This provided an observational diagnostic of an AM CVn system's initial conditions. The Deloye et al. (2005) calculation also indicated that WD channel systems with hot donors and He-star channel systems would not be distinguishable based on \dot{M} determinations alone.

Since the entropy structure of the donor determines its response to mass loss (see the discussion in §4.1.1 and Appendix A), assuming a fully convective structure will overestimate the binary's P_{orb} evolution rate if the donor's

true structure is not adiabatic. Further, while assuming the donor responds adiabatically to mass-loss is certainly valid at early stages of the AM CVn phase when \dot{M} is very large, this assumption may break down as the binary evolves outward in P_{orb} to lower \dot{M} .

To rectify these shortcomings and provide predictions for the donor's luminosity and effective temperature, we undertook a study to model the donors within the context of a full stellar structural calculation coupled to the evolution of the AM CVn binary. In particular, we sought to determine the donor's observational signatures as a function of initial system parameters and P_{orb} , as well as to determine how a complete treatment of the donor's structure alters the conclusions of earlier studies. We also sought to model accurately the critical phase of mass transfer turn-on, when the donor is coming into contact and a transition in the P_{orb} -evolution from GW-dominated in-spiral to the mass-transfer dominated expansion occurs. This phase of WD channel system evolution has not been modelled in any detail prior to this study.

To carry out the computations, we developed a new stellar evolution code to perform the coupled donor/binary calculations. A brief description of this code, detailing our numerical modelling of the donor and binary is provided in §2. In §3, we describe the procedure for determining the range of initial donor degeneracy and donor structural models used for our AM CVn phase calculations. We present the results of our calculations in §4 and discuss these results and several of their applications in §5. Finally, we summarize in §6.

2 DETAILS OF OUR NUMERIC CALCULATIONS

To achieve a necessary level of flexibility in terms of input physics and defining system of equations for this and related projects, we implemented a stellar evolution code capable of handling most 1D stellar evolution calculations expressed as boundary-value problems. This code is written in C++ and is comprised of a suite of abstract classes defining the necessary components of a stellar evolution calculation. At its core is a generalized 1D relaxation-method boundary-value problem (BVP) solver (see, e.g, §17.3 of Press et al. 1992) that utilizes the sparse-matrix solver UMFPACK² to perform the necessary matrix inversions. The defining system of ordinary differential equations (ODEs) and necessary input physics are implemented as separate abstract classes, providing the desired flexibility. Utilizing this new code, we solve for both the donor's structure and binary parameters within a single set of relaxation iterations at each time step. Below we detail our numerical treatment for both components of our system and describe the input physics.

2.1 Calculation of the Donor's Structure

For the donor, we solve the standard set of 1D hydrostatic stellar structure equations augmented by an automatic mesh

² <http://www.cise.ufl.edu/research/sparse/umfpack/>

allocation algorithm (Eggleton 1971) on a 200-point non-lagrangian mesh:

$$\frac{d \ln P}{dm} = -\frac{Gm^2}{4\pi r^4 P}, \quad (1)$$

$$\frac{d \ln T}{dm} = \nabla \frac{d \ln P}{dm}, \quad (2)$$

$$\frac{d \ln r}{dm} = \frac{1}{4\pi r^3 \rho}, \quad (3)$$

$$\frac{dl}{dm} = \epsilon - c_P \left(\frac{\partial T}{\partial t} - \nabla_{\text{ad}} \frac{T}{P} \frac{\partial P}{\partial t} \right), \quad (4)$$

$$\frac{dq}{dm} = \frac{1}{\theta} \left(-\alpha_1 \frac{\ln P_c}{\ln P_e} \frac{d \ln P}{dm} + \frac{\alpha_2}{m} \right). \quad (5)$$

Here ρ , T , P , r , and l , are the density, temperature, pressure, radius, and luminosity at each mesh point, m is the mass interior to each mesh point, t is time, ϵ is the local nuclear energy generation rate (which we set to zero throughout this work), and c_P is the specific heat at constant pressure. In equation (5)—which determines the mesh allocation— P_c and P_e are the pressures at the stellar centre and exterior point, respectively, α_1 , α_2 are constants that weight the importance of pressure and mass gradients in determining the mesh spacing, and θ is an overall normalization constant determined implicitly at each time step. The quantity $\nabla_{\text{ad}} \equiv (d \ln T / d \ln P)_s$, where s is the specific entropy, and $\nabla \equiv d \ln T / d \ln P$ describes the actual run of T with P within the donor. We take $\nabla = \nabla_{\text{rad}}$ when $\nabla_{\text{rad}} < \nabla_{\text{ad}}$, where

$$\nabla_{\text{rad}} \equiv \frac{3}{16\pi acG} \frac{P \kappa l}{T^4 m}, \quad (6)$$

and κ is the Rosseland mean opacity. Otherwise we determine ∇ using mixing length theory with the mixing length set equal to one pressure scale height.

The central boundary conditions are determined by the standard central expansions of the stellar structure equations. At the outer boundary, we equate the values of the iterated quantities at the outermost mesh point, T_e , P_e , r_e , l_e , and m_e with the corresponding values at the photosphere (i.e., we do not calculate a separate atmosphere model). Grey atmospheres and the Eddington approximation are assumed. The photospheric pressure is therefore given by:

$$P_{\text{phot}} = \frac{2}{3} \frac{GM_2}{R_2^2 \kappa_{\text{phot}}}, \quad (7)$$

where $\kappa_{\text{phot}} = \kappa(\rho_{\text{phot}}, T_{\text{eff}})$, ρ_{phot} is the photospheric density, and T_{eff} is the donor's effective temperature. This gives the matching conditions $T_e = T_{\text{eff}}$, $P_e = P_{\text{phot}}$, $r_e = R_2$, and $m_e = M_2$, and $l_e = L$. Here M_2 , R_2 and L are the donor's total mass, radius, and luminosity, with $L = 4\pi\sigma R_2^2 T_{\text{eff}}^4$.

To produce a smoothly varying outer boundary condition, equation (7) is not solved directly each time photospheric values are required. Instead, a 3×3 grid of $(T_{\text{eff}}, g = GM_2/R_2^2)$ points is constructed that straddle the donor's current photospheric conditions. We calculate P_{phot} from equation (7) at these values and use these to determine P_{phot} by cubic-spline interpolations during the iterations. If a point outside of the current grid is needed, the grid is re-centred and new P_{phot} values calculated. The T_{eff} and g grids have spacings $\Delta \log(T_{\text{eff}}/K) = 0.05$, $\Delta \log(g/\text{cm s}^{-2}) = 0.05$.

2.2 Calculation of the Binary Parameters

To specify the binary system, we add the following three equations to the above set of ODEs:

$$\frac{d \ln M_2}{dt} = \frac{\dot{M}_2}{M_2} = -\frac{\dot{M}}{M_2}, \quad (8)$$

$$\frac{d \ln M_1}{dt} = \frac{\dot{M}_1}{M_1}, \quad (9)$$

and

$$\begin{aligned} \frac{d \ln a}{dt} = & 2 \frac{\dot{J}}{J} - \frac{1}{M_1 + M_2} \\ & \times \left[\frac{\dot{M}_1}{M_1} (M_1 + 2M_2) + \frac{\dot{M}_2}{M_2} (M_2 + 2M_1) \right], \quad (10) \end{aligned}$$

where M_1 is the accretors mass, a is the orbital separation, J is the orbital angular momentum. The quantities \dot{M}_1 , \dot{M}_2 specify the mass evolution rate of the accretor and donor; both are, in general, functions of the binary's and, possibly, the donor's state. We express the a evolution in the form of equation (10) to allow for this generality. However, here, we consider conservative mass transfer, setting $\dot{M}_1 = \dot{M} = -\dot{M}_2$ always. We consider only gravity wave emission (Landau & Lifshitz 1971) contributions to the J evolution, ignoring the possibility of accretor spin-up in the J evolution. This latter effect may play a significant role in determining whether an AM CVn binary survives the onset of contact (Nelemans et al. 2001; Marsh et al. 2004). This omission is justified since we are interested in understanding the parameter space potentially allowed to AM CVn systems, not in a detailed characterization of the actual, realized population. This latter question will be the subject of future studies.

To determine \dot{M}_2 we utilize the prescriptions of Ritter (1988) and Kolb & Ritter (1990). Specifically, when the donor's Roche radius, R_L , here calculated as (Paczynski 1967)

$$R_L \approx 0.46a \left(\frac{M_2}{M_1 + M_2} \right)^{1/3}, \quad (11)$$

(valid for $q \equiv M_2/M_1 \leq 0.8$) is larger than R_2 , the mass loss is modelled as an isothermal flow of a classical gas with a rate

$$-\dot{M}_2 = \dot{M}_0 \exp \left(\frac{\Delta R}{H_P} \right) \quad (12)$$

where $\dot{M}_0 > 0$ is the mass transfer rate off the donor when $R_2 = R_L$ and depends on the surface properties (Ritter 1988), H_P is the pressure scale height at the photosphere, and $\Delta R = R_2 - R_L$. When $R_L < R_2$, we model the sub-photospheric contributions with an adiabatic flow (Kolb & Ritter 1990). To do so, we rewrite equation (A17) of Kolb & Ritter (1990) in a more general form to allow for degeneracy or non-ideality:

$$-\dot{M}_2 = \dot{M}_0 + 2\pi F_1(1/q) \frac{R_L^3}{GM_2} \int_{(R_2 - \Delta R)}^{R_2} F_2(\Gamma_1) \frac{Gm(P\rho)^{1/2}}{r^2} dr \quad (13)$$

where F_1 and F_2 are defined in Kolb & Ritter (1990) and $\Gamma_1 = (\partial \ln P / \partial \ln \rho)_s$. We determine \dot{M} implicitly at each timestep, a method that greatly improves the numerical stability (Büning & Ritter 2006).

2.3 Input Physics

For the donor’s composition, we assume a fixed, homogeneous mixture with He, C, N, and O mass fractions of 0.981, 1.41×10^{-4} , 0.0122, and 1.06×10^{-3} (typical of the core composition of solar metallicity stars at the base of the red-giant branch that have undergone CNO-cycle burning; Schaller et al. 1992; Girardi et al. 2000). The remaining metals are assumed to have a solar abundance pattern. We use OPAL radiative opacities (Iglesias & Rogers 1996) calculated for this mixture for temperatures above 10^4 K. Below 10^4 K, we use Ferguson et al. (2005) opacities calculated *excluding* contributions due to grains (which form beginning at $T \approx 2500$ K). Where conductive opacities are relevant, we utilize those of Potekhin et al. (1999). As metals make negligible contributions to the donor’s EOS (Chabrier & Baraffe 1997), the pure-He EOS of Winisdoerffer & Chabrier (2005) supplemented by radiation contributions are used. This EOS is calculated using a free-energy minimization model and provides the thermodynamic quantities of a He fluid over a wide range of density and temperature including, in particular, the regimes where He undergoes thermal and pressure ionization state transitions.

3 THE INITIAL STATE OF THE DONOR IN WHITE DWARF CHANNEL SYSTEMS

As shown in Deloye et al. (2005), evolution during the post-contact AM CVn phase is strongly influenced by the state of the donor at contact. In this section, we determine a set of initial donor models that encompass the range of donor properties at contact produced in WD channel AM CVn systems and discuss the expected distribution of these properties based on the population synthesis calculation of Nelemans et al. (2001).

3.1 Determination of the Initial Donor Models

To determine the range of parameters our initial donor models should cover, we utilize data from the Nelemans et al. (2001) population synthesis model and the methodology of Deloye et al. (2005). Specifically, for each WD channel system in the population synthesis model that is expected to survive initial contact (see Nelemans et al. 2001), we determine the proto-donor’s core conditions at the beginning of the second CE using existing stellar evolution calculations performed with the EZ code (Paxton 2004) for the Deloye et al. (2005) study. During the rapid CE phase, the proto-donor’s central degeneracy doesn’t change. So we utilize the central degeneracy parameter— $\psi_c = E_{F,c}/kT_c \approx \rho_c / (1.2 \times 10^{-8} T_c^{3/2}) K^{3/2} \text{ cm}^3 \text{ g}^{-1}$, where ρ_c , T_c , $E_{F,c}$ are the central density, temperature, and electron Fermi energy—to map between the EZ stellar models pre-CE and a set of post-CE isolated He WD models calculated using with our own stellar evolution code.

Once we determine this post-CE donor model, for each system we evolve the donor’s radius and the orbital separation from this post-CE state to determine when GW emission drives the binary back into contact. The population synthesis data provides the post-CE orbital separation, a_0 , and the initial accretor and donor masses, $M_{1,i}$ and $M_{2,i}$.

We use these quantities and our single He-star tracks to calculate, self-consistently, the time elapsed in the post-CE phase, t_{contact} , before $R_2 = R_L$. This determines the donor’s contact radius and ψ_c (which we denote by $R_{2,i}$ and $\psi_{c,i}$). When taken over the set of population synthesis data, this procedure allows us to determine the range of $\psi_{c,i}$, $M_{2,i}$, and $M_{1,i}$ that occurs in the WD channel systems.

Before discussing the distribution of donor contact parameters obtained with this procedure, we mention one complication we encountered. In some systems, the standard CE-evolution prescription (see, e.g., Webbink 1984) predicts post-CE conditions where *the donor is already in Roche contact*. This is due to some systems having sufficiently hot proto-donors with R_2 significantly greater than the zero-temperature configuration. It is unclear whether such systems will cleanly exit the CE or simply be driven to a prompt merger.

A realistic determination of this question is beyond the scope of this paper. Instead, in order to examine how this issue could influence the distribution of donor contact parameters, we considered two different, *rough* criteria for determining which systems survive the CE. In one, we removed all such systems from the population. In the second, we looked at the evolution of R_2 (based on the *isolated* He WD structures) and R_L to determine if $R_2 < R_L$ was ever satisfied before the system was driven to $a = 0$ due to GW emission. This could happen if the proto-donor is able to contract more rapidly than GW emission decreases R_L .

We found that the choice of criteria effected mainly the distribution of $\psi_{c,i}$ at fixed $M_{2,i}$ for systems with $M_{2,i} \leq 0.175M_\odot$. Taking the second criteria, About 50% of systems with $0.10M_\odot < M_{2,i} \leq 0.125M_\odot$ and 25% of those with $0.125M_\odot < M_{2,i} \leq 0.175M_\odot$ do not exit the CE by this rough criteria, where as only 4% of those with $M_{2,i} > 0.175M_\odot$ are affected. More importantly, the range of $\psi_{c,i}$ in the overall population is not affected by these border line systems, since donors with $M_{2,i} \gtrsim 0.2M_\odot$ exhibit the full range of $\psi_{c,i}$ and these more massive donors all appear to exit the CE cleanly. This general conclusion also applies to concerns about donors with $M_{2,i} \approx 0.1M_\odot$. The progenitors of these donors will not have developed a distinct core/envelope structure at the start of the CE, making it unlikely that they will survive the CE-event (Taam & Sandquist 2000). Thus, excluding such systems from consideration will also not influence the $\psi_{c,i}$ range expected in this population.

3.2 The Distribution of Initial Donor Parameters

The results of the above exercise produces a population with $M_{2,i} \approx 0.1 - 0.325M_\odot$ and $\log(\psi_{c,i}) \approx 1.0 - 4.0$ (i.e., donors are mildly to extremely degenerate). Our determination of the donor’s ρ_c , T_c at contact for each system in the Nelemans et al. (2001) population synthesis model, is shown in Figure 1 by crosses. Each cross represents the starting point for a number of systems, so the density of crosses does not correspond to the number of systems starting within a given region of this parameter space. Dashed lines show lines of constant ψ_c , while solid curves show the evolution along our isolated He WD tracks. We have excluded systems not exiting the CE according to our second criteria above from this plot; if we were to use the first criteria, the

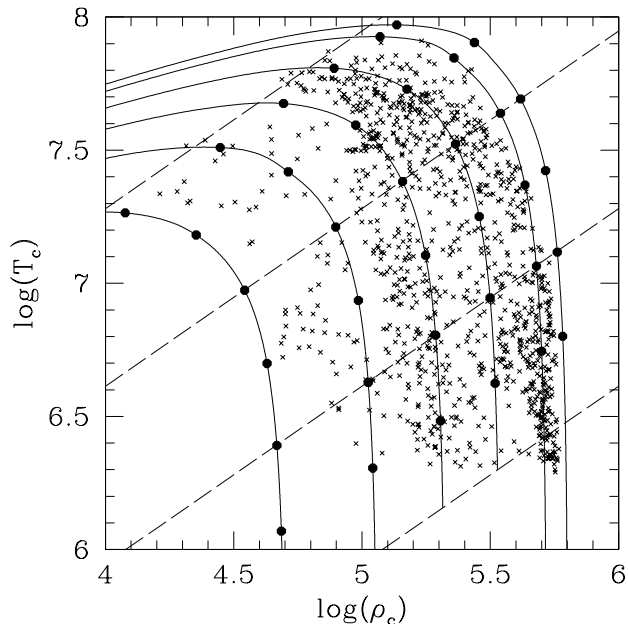


Figure 1. The donors’ ρ_c , T_c at contact for each WD channel AM CVn system in the Nelemans et al. (2001) population synthesis model (crosses). For comparison, the solid lines show the ρ_c , T_c evolution along each of our isolated He-star evolution tracks (with M_2 values of, from bottom to top, 0.10, 0.15, 0.20, 0.25, 0.30, and $0.325 M_\odot$). Lines of constant $\log \psi_c = 1.0, 2.0, 3.0,$ and 4.0 are shown by the dashed lines (top to bottom). The solid circles show the central conditions of the set of initial donor models used to begin our AM CVn phase calculations.

only change here would be the loss of most systems with $0.1 \lesssim M_{2,i} \lesssim 0.15 M_\odot$ and $1.0 \lesssim \log(\psi_{c,i}) \lesssim 1.5$. The solid circles in this figure show the central conditions of the initial donor models we use in subsequent calculations.

We show the distribution in orbital period, P_{orb} , at contact (integrated over all $M_{2,i}$) in Figure 2 with the solid line. In this plot, the number, N , in each bin represent the total number of WD channel AM CVn systems in the Nelemans et al. (2001) population synthesis model that make contact within each P_{orb} range. For comparison we also show with the dashed line the distribution that results from assuming fully degenerate donors. We take P_{orb} at contact to equal $53.5(R_{2,i}/0.1R_\odot)^{3/2}(M_{2,i}0.1M_\odot)^{-1/2}$ minutes and calculate the fully degenerate $R_{2,i}$ using a fit to the Deloye & Bildsten (2003) zero-temperature He mass-radius relation:

$$R_{2,\text{DB}} = 0.005593 - \frac{1.7616 \times 10^{-5}}{M_2} + 0.004643 M_2 - 0.008298 \ln M_2, \quad (14)$$

which is accurate to better than 3% over the range $9 \times 10^{-4} M_\odot \leq M_2 \leq 0.45 M_\odot$. The fully degenerate distribution peaks at $P_{\text{orb}} = 3.0$ minutes with a cut-off at 6 minutes. On the other hand, roughly 25% of systems within our current calculation make contact at a $P_{\text{orb}} > 6$ minutes and 5% at $P_{\text{orb}} > 11$ minutes. Additionally, there is a small tail of systems making contact out to $P_{\text{orb}} = 35$ minutes (not shown in Figure 2). If we remove all systems with post-CE

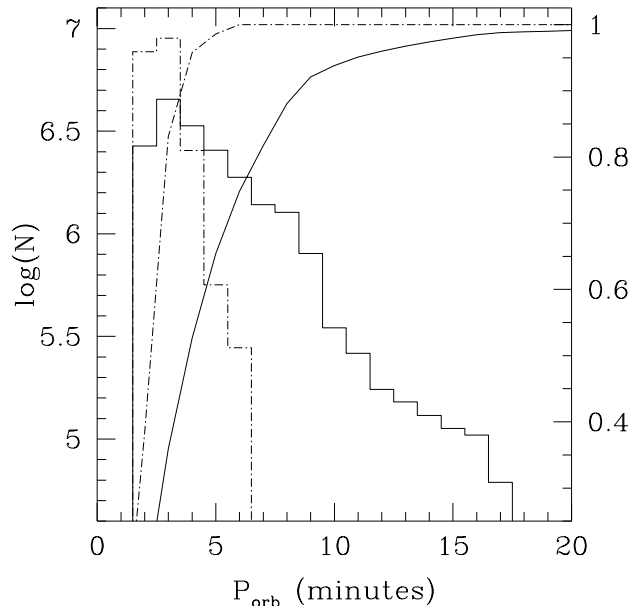


Figure 2. The contact P_{orb} -distribution as determined by self-consistent treatment of the donor’s cooling before contact (solid histogram) compared to assuming all donors are fully degenerate at contact (dash dotted histogram). The number of systems in each bin gives the total number of current WD channel AM CVn systems in the Nelemans et al. (2001) population synthesis model whose contact P_{orb} fell within each bin. The solid and dashed curves show the corresponding cumulative fractional distribution of contact P_{orb} .

$R_L < R_2$, this tail extends out to 22 minutes, but otherwise the contact P_{orb} -distribution is almost unchanged.

The corresponding $\psi_{c,i}$ -distribution is shown by the histogram in Figure 3. The solid curve in this figure gives the cumulative distribution of $\psi_{c,i}$ values. Noteworthy is the fact that, unlike the contact P_{orb} -distribution, which is strongly biased towards short P_{orb} , the $\psi_{c,i}$ -distribution is approximately flat between $\log(\psi_{c,i}) \approx 1.4$ and 3.6 . The difference in the two distributions is due to the dependence of R_2 on $\psi_{c,i}$: R_2 varies rapidly with $\psi_{c,i}$ for $\psi_{c,i} \sim 1 - 10$, but only more slowly for $\psi_{c,i} \gtrsim 100$. Thus there is not as strong an a priori theoretical preference for large $\psi_{c,i}$ values in the WD channel population as might be expected from the contact P_{orb} -distribution. The $\psi_{c,i}$ -distribution is essentially unchanged when removing all systems with post-CE $R_L < R_2$ from consideration.

4 THE DONOR’S STRUCTURAL AND THERMAL EVOLUTION

In order to adequately sample the range of initial donor properties derived in §3 in our subsequent calculations, we considered AM CVn evolution starting from 36 different initial donor models (solid circles in Fig. 1) with $M_{2,i}$ values of 0.10, 0.15, 0.20, 0.25, 0.30, and $0.325 M_\odot$ and $\log(\psi_{c,i})$ values of 1.1, 1.5, 2.0, 2.5, 3.0, and 3.5. The coupled binary and donor evolution were calculated for two $M_{1,i}$ for each donor model. These $M_{1,i}$ were chosen so that $M_{\text{tot}} = M_{2,i} + M_{1,i}$ equalled one of three values—0.5, 0.825, or $1.325 M_\odot$.

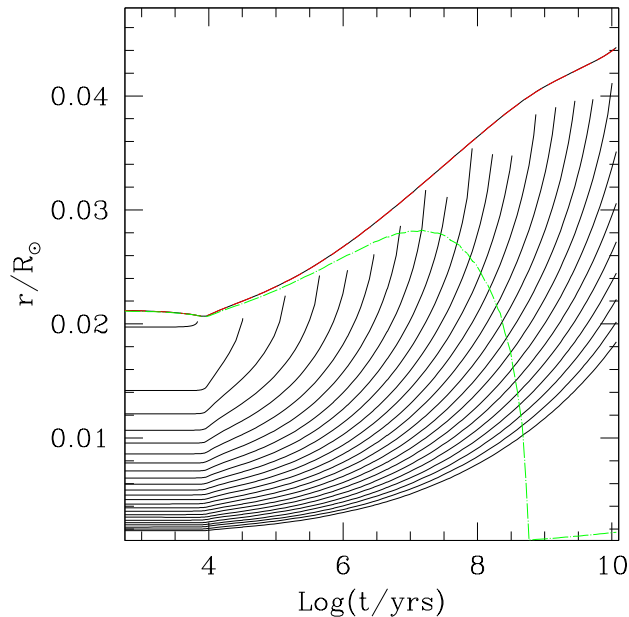


Figure 5. Same as Figure 4, but with a more degenerate donor; the initial conditions in this system are $M_{2,i} = 0.2 M_{\odot}$, $\log(\psi_{c,i}) = 3.5$, $R_{2,i} = 0.0212 R_{\odot}$, and $M_{1,i} = 0.3 M_{\odot}$

continues to cool (evolution beyond $t \approx 2 - 3 \times 10^9$ yrs in Fig. 4).

The first and third phases of the donor’s evolution are qualitatively new results resulting from our more complete treatment of the donor’s physics. A more detailed discussion of these phases follows.

4.1.1 The \dot{M} Turn-on Phase: Evolution to \dot{M} -Maximum

Once the WD channel AM CVn donors make contact, our calculations show they all begin a phase of radius contraction, a result not anticipated by prior modelling (e.g., Nelemans et al. 2001; Deloye et al. 2005). Here, we discuss how the donor’s structure determines the duration and extent of this initial R_2 contraction phase.

The basic picture of the donor’s response to mass loss can be seen from Figs. 4 and 5. As M_2 decreases, mass elements move to lower P and ρ , producing the expansion in r at fixed m seen in the evolution of the interior black lines. In Appendix A we show that this expansion is most significant near the surface and that the only contribution to R_2 contraction comes from the surface term in equation (A2). In other words, mass lost from the donor takes with it its contribution to R_2 , tending to produce contraction. The overall R_2 evolution then depends on whether the underlying layers expand sufficiently to compensate for this lost radius contribution.

Equation (A5) shows that this underlying expansion depends on the two quantities: $\chi_T \equiv (\partial \ln P / \partial \ln T)_{\rho}$ and $\nabla - \nabla'$, where $\nabla' = (\partial \ln T / \partial \ln P)_m$ describes the actual thermal evolution of a mass element as it is advected to lower P . In layers where either of these quantities tends towards zero, the $\rho(P)$ profile remains constant under advection, producing no net change in the relative contribution to R_2 from that region. This can occur for strongly degenerate plasmas,

where $\chi_T \approx 0$, or when the advected mass element arrives at a lower P with the same entropy as the material it replaces. Only when the advected mass elements arrive with lower entropy ($\nabla' > \nabla$) is the relative R_2 contribution reduced. If the latter case dominates in the outer layers, this can lead to a net decrease in R_2 .

Degeneracy effects never dominate in our donors outer layers—at least during this contact phase—so the R_2 evolution depends only on the mode of heat transport in the outer layers and on the ordering of τ_{th} and τ_m . When $\tau_{th} \ll \tau_m$, heat transport has sufficient time to redistribute entropy so that $\nabla' \approx \nabla$, and little R_2 evolution occurs. Once $\tau_m \lesssim \tau_{th}$, so that $\nabla' \rightarrow \nabla_{ad}$, the R_2 evolution begins to depend on the background entropy gradient. In convective regions, ∇ is essentially equal to ∇_{ad} , so that adiabatic advection leads to minimal local contributions to R_2 evolution. In radiative regions, however, $\nabla < \nabla_{ad}$; thus only for radiative surface regions during roughly adiabatic advection will a net R_2 -contraction occur (see, e.g., Faulkner 1976, for another, qualitative, discussion of this). The rate of the R_2 contraction increases with the entropy of the layer and with the steepness of the background entropy profile.

The structure of our donor’s outer layers consists of a superficial radiative layer overlying a thin outer-convective zone, followed by another radiative region that extends to the stellar centre. The thickness of outer-convective region increases with donor degeneracy. The entropy profile of the inner radiative region is very steep near its outer boundary; moving inward, this entropy profile tends to flatten out rather abruptly. With this general interior structure in mind, the R_2 evolution trends seen in Figs. 4 and 5 can be understood from the above discussion.

For the $\log(\psi_{c,i}) = 2.0$ donor (Fig. 4), as long as $\tau_{th} \ll \tau_m$, the R_2 evolution is minimal. Once this inequality is reversed, the R_2 evolution starts to accelerate and a rapid contraction ensues due to the steep entropy profile in the donor’s radiative photosphere. By this time, the underlying layers are advected nearly adiabatically, and the entropy gradient near the surface is continuously decreasing. This leads to the decreasing rate of R_2 contraction. Finally the entropy profile becomes sufficiently shallow that the expansion of the underlying layers takes over, and R_2 begins increasing.

The evolution in Fig. 5 is similar, but here the evolution is adiabatic ($\tau_{th} \gg \tau_m$) throughout. The R_2 contraction rate is slower both because the outer convective zone is thicker and the underlying radiative region has both a lower entropy and a shallower entropy profile. This also results in less overall R_2 contraction. Additionally, R_2 decreases significantly only once a sufficient amount of mass, δm , has been lost for the pressure perturbation in the outer layers, $\delta P \approx GM_{2,i} \delta m / (4\pi R_{2,i}^4) \approx 9 \times 10^{20} \text{ dyne cm}^{-2} (\delta m / M_{2,i}) (M_{2,i} / 0.1 M_{\odot})^2 (0.01 R_{\odot} / R_{2,i})^4$, to be of order the initial P at the top of the radiative region.

The relative rate of R_2 and R_L evolution—characterized by $\xi_{R_2} \equiv (d \ln R_2 / d \ln M_2)$ and $\xi_{R_L} \equiv (d \ln R_L / d \ln M_2)$ —determines that of \dot{M} . In all our evolution models, $\xi_{R_L} \gg \xi_{R_2}$ initially. However, since

$$\xi_{R_L} = 2 \left[\left(\frac{J}{J} \right)_{\text{GW}} \frac{M_2}{M_2} + q - \frac{5}{6} \right], \quad (17)$$

ξ_{R_L} rapidly decreases with growing \dot{M} . Once $\xi_{R_L} \approx \xi_{R_2}$,

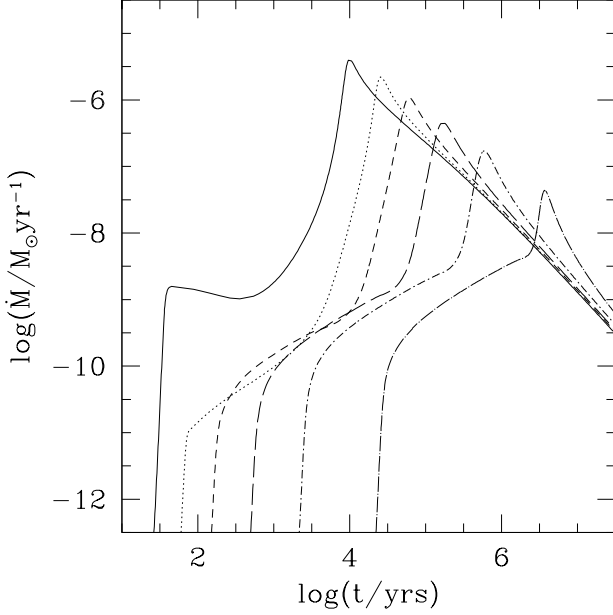


Figure 6. The $\dot{M}(t)$ evolution for AM CVn systems with $M_{2,i} = 0.2$ and $M_{1,i} = 0.3M_{\odot}$. Systems with donors having $\log(\psi_{c,i}) = 3.5, 3.0, 2.5, 2.0, 1.5,$ and 1.1 are shown by the solid, dotted, short-dashed, dashed, short-dash dotted, and dash dotted lines, respectively. The corresponding $R_{2,i} = 0.0212, 0.0225, 0.0248, 0.0294, 0.0380, 0.0561 R_{\odot}$, respectively

these two quantities tend to track each other closely due to the sensitive ΔR dependence of \dot{M} . Thus, when the ξ_{R_2} evolution is smooth, the \dot{M} evolution is also.

This can be seen in Figure 6, which shows the \dot{M} time evolution for a set of models with $M_{2,i} = 0.2$, $M_{1,i} = 0.3M_{\odot}$ and differing $\psi_{c,i}$ (indicated by line style with $\psi_{c,i}$ decreasing left-to-right). The four lowest $\psi_{c,i}$ donors have very thin outer convective zones and their corresponding ξ_{R_2} evolution is smooth. The two highest $\psi_{c,i}$ donors (dotted and solid curves) have their R_2 response dominated, at first, by their thicker outer convective zones. Once δm begins probing the underlying radiative region, their ξ_{R_2} suffer rapid changes in slope. This transition from convective to radiative dominated R_2 response produces the non-smooth and non-monotonic behaviour seen in the dotted and solid curves.

Figure 6 illustrates other general trends. Initially, $R_L > R_2$ in all cases. While this remains true, the \dot{M} growth is approximately exponential (corresponding to the initial, steep increase in \dot{M}). Lower $\psi_{c,i}$ donors produce slower \dot{M} growth both due to their larger contact a (reducing the system's \dot{J}/J) and larger H_P/R_2 ; the latter tends to be the more significant factor. Since the \dot{M} required to produce $\dot{a} > 0$ is greater than \dot{M}_0 in all the systems we considered, all experience a phase where $R_L < R_2$. Once this occurs, the \dot{M} growth slows as \dot{M} now depends on the donor's non-exponential, sub-photospheric ρ -profile (see equation 13). This results in the turn-over in \dot{M} growth seen at $\dot{M} \sim 10^{-10}$ - $10^{-9} M_{\odot} \text{ yr}^{-1}$. The final upturn in \dot{M} before each maximum results from a rapid increase in \dot{M}_0 via the increasing ρ of the surface layers. This results from the adiabatic advection of lower entropy material to the surface

and corresponds to the final phase of rapid R_2 contraction discussed above.

The extrema in R_2 , a , and \dot{M} , which mark the end of the turn-on phase, do not occur simultaneously. The R_2 -minimum happens first and the subsequent expansion contributes to accelerating the \dot{M} growth. The a -minimum occurs once \dot{M} reaches a critical value, $\dot{M}_{\text{crit}} = -(\dot{J}/J)_{\text{GW}} M_2 / (1 - q)$ to produce $\dot{a} = 0$. The larger \dot{J}/J_{GW} in systems with more degenerate donors produces higher \dot{M}_{crit} . Eventually, the a -expansion leads to a decreasing ΔR , and \dot{M} reaches its maximum. By \dot{M} -maximum, the donor has lost between $\delta m \approx (0.02 - 0.2) M_{2,i}$. Less degenerate donors suffer the greater mass loss. Overall the turn-on phase lasts between $\sim 10^4$ and $\sim 10^6$ yrs.

4.1.2 The Donor's Cooling Phase

By the time the system has evolved past \dot{M} -maximum, the donor is evolving adiabatically in response to mass loss. Prior work on the evolution of AM CVn systems in this phase has neglected the donor's thermal evolution and has either relied on predetermined M - R tracks (Nelemans et al. 2001; Farmer & Phinney 2003) or has assumed the donors continue to evolve adiabatically indefinitely (Deloye et al. 2005). Our current calculations show that at late-times, the assumption of adiabatic evolution becomes invalid (as can be seen by the evolution of $\tau_m = \tau_{\text{th}}$ in Fig. 4).

Why the donor's adiabatic evolution ends can be understood by considering how τ_m and τ_{th} evaluated at $m' = M_2$ evolve under mass loss. The quantity

$$\left. \frac{d \ln \tau_m}{d \ln M_2} \right|_{m'=M_2} = 1 - \frac{d \ln \dot{M}}{d \ln M_2}. \quad (18)$$

For GW driven, conservative mass transfer, the latter derivative can be written as

$$\frac{d \ln \dot{M}}{d \ln M_2} = 2 - q - 4 \frac{d \ln a}{d \ln M_2} \approx 2 - 4 \left(\xi_{R_2} - \frac{1}{3} \right), \quad (19)$$

where the final approximation is good when $M_2 \ll M_1$. In the same regime,

$$\left. \frac{d \ln \tau_m}{d \ln M_2} \right|_{m'=M_2} \approx 4 \left(\xi_{R_2} - \frac{1}{3} \right) - 1. \quad (20)$$

It is useful to rewrite $\tau_{\text{th}} = \int_0^{M_2} c_P T dm' / L$ as $c'_P T_c M_2 / L$ where $c'_P = \int_0^{M_2} c_P T dm' / (T_c M_2)$ since both c'_P and L vary only by a factor of a few during the adiabatic phase. In contrast, M_2 and T_c vary by roughly one and two orders of magnitude, respectively. Holding c'_P , L constant, $d \ln \tau_{\text{th}} / d \ln M_2 \approx 1 + d \ln T_c / d \ln M_2$, and we can use hydrostatic balance to write

$$\left. \frac{d \ln T_c}{d \ln M_2} \right|_{m'=M_2} = \left(\frac{d \ln T_c}{d \ln P_c} \right) \left(\frac{d \ln P_c}{d \ln M_2} \right) = \nabla_{\text{ad},c} (2 - 4\xi_{R_2}), \quad (21)$$

where $\nabla_{\text{ad},c}$ characterizes the T_c evolution during the adiabatic phase.

Thus once $M_2 \ll M_1$ in the adiabatic phase, $\tau_{\text{th}}/\tau_m \propto M_2^\alpha$ where

$$\alpha = 4\xi_{R_2} - \frac{10}{3} + \nabla_{\text{ad},c} (4\xi_{R_2} - 2). \quad (22)$$

Typically, $\xi_{R_2} \approx -0.3$ - -0.2 and $\nabla_{\text{ad},c} \approx 0.36$ - 0.39 , so that $\alpha \approx -5.7$ - -5.2 and leading a rapid evolution of τ_{th}/τ_m as

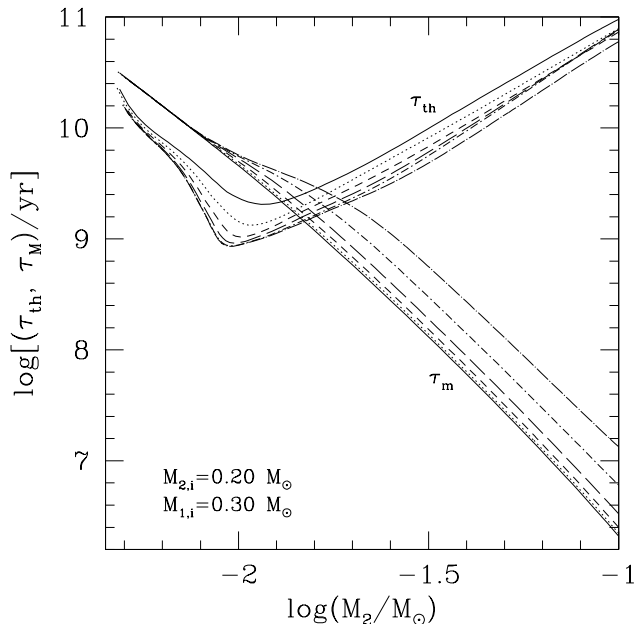


Figure 7. The evolution of τ_{th} and τ_{m} (at $m' = M_2$) as a function of M_2 for the set of AM CVn models with $M_{2,i} = 0.2M_{\odot}$ and $M_{1,i} = 0.3M_{\odot}$ shown in Fig 6. The various lines styles have the same meaning as in that figure.

M_2 is reduced. In the early portion of the adiabatic phase, where $M_2 \sim 0.1M_{\odot}$, $\tau_{\text{th}}/\tau_{\text{m}} \sim 10^3 - 10^5$ and this scaling then gives $\tau_{\text{th}}/\tau_{\text{m}} \approx 1$ when $M_2 \approx 0.01 - 0.03M_{\odot}$.

We compare this prediction to our numerical calculations in Fig. 7, where we show the computed evolution of both time-scales for our models with $M_{2,i} = 0.2M_{\odot}$, $M_{1,i} = 0.3M_{\odot}$. The ratio $\tau_{\text{th}}/\tau_{\text{m}} \approx 1$ at $M_2 = 0.01 - 0.02$ in all cases, in excellent agreement with the scaling relation. Beyond this point, the donor is able to shed entropy, allowing less degenerate donors to contract towards a fully degenerate configuration.

4.2 Impact of Initial Conditions on Donor Evolution

We now explore how the donor and binary evolution varies with initial conditions. In Fig. 8, we show the $R_2(M_2)$ evolution for several sets of calculations. In this figure, different colours correspond to different initial donor degeneracy, while different line styles indicate different M_{tot} . The evolution along each track is from right to left, with the donors first evolving steeply downward in R_2 . The amount R_2 decreases prior to the R_2 -minimum depends on $\psi_{c,i}$. Less degenerate donors contract to a greater extent during the turn-on phase as discussed in §4.1.1.

In panel (a) of Fig. 8 the R_2 evolution for a set of systems with $M_{\text{tot}} = 0.825M_{\odot}$ are displayed. During the turn-on phase and early expansion phase, $R_2(M_2)$ depends on both $\psi_{c,i}$ and $M_{2,i}$. At fixed $\psi_{c,i}$ different $M_{2,i}$ have differing $s(m)$ profiles, and this is reflected in the R_2 evolution. The entropy differences are more significant at larger m , producing the tendency towards convergence as M_2 is reduced. Near the local R_2 -maximum (at $M_2 \approx 0.01 - 0.03$), track convergence is furthered by donor cooling, which erases any

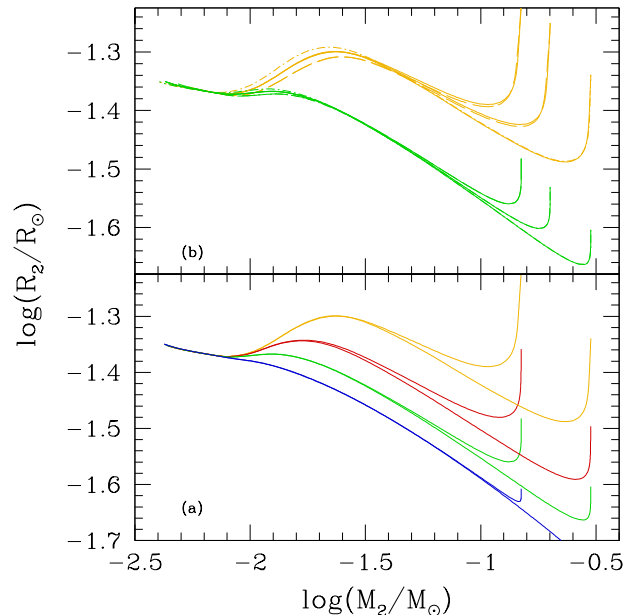


Figure 8. The dependence of the R_2 -evolution on initial binary parameters. In both panels, colours indicate the donor's initial $\log(\psi_{c,i})$: 1.1 (yellow), 1.5 (red), 2.0 (green), and 3.0 (blue). Line style indicates the binary's M_{tot} : 0.500 (dashed), 0.825 (solid), and 1.325 M_{\odot} (dot short-dashed). Panel (a) compares the R_2 - M_2 evolution for systems with $M_{\text{tot}} = 0.825M_{\odot}$ to examine the impact of initial degeneracy and donor mass. We show evolution for systems with $M_{2,i} = 0.15$, and $0.3 M_{\odot}$ and the initial degeneracy listed above. Panel (b) examines the impact of varying M_{tot} on the R_2 evolution. We show comparisons at two $\psi_{c,i}$ to illustrate how the magnitude of M_{tot} effects are reduced at higher donor degeneracy.

remaining initial s -profile information. By this point, the donors cool and contract along tracks parametrized by $\psi_{c,i}$. Cooling continues and R_2 contraction slows as the donors become increasingly degenerate and finally reach the fully degenerate M - R relation.

In panel (b) of Fig. 8, we consider the dependence of the R_2 evolution on M_{tot} . During the turn-on phase, the donor evolution is essentially independent of M_{tot} . Only for the very lowest degeneracy donors is this not the case. These donors are able to cool somewhat during the turn-on phase and systems with lower M_{tot} produce slower \dot{M} growth, allowing greater cooling before mass loss becomes adiabatic. The larger \dot{M} in higher M_{tot} systems also extends the duration of the adiabatic expansion phase to lower M_2 and larger R_2 . The R_2 path a system follows during its later contraction phase is thus parametrized by $\psi_{c,i}$ and M_{tot} .

In Fig. 9 the evolution of the donor's L is shown as a function of P_{orb} , with evolution proceeding downward along each track. The L -evolution reflects the donor's evolutionary stages. The significant decrease during the turn-on phase (while P_{orb} is decreasing) is due primarily to the removal of mass from the steep s -profile region (see Appendix B). Once the steep s -gradient material has been removed, the L evolution slows along with the R_2 contraction. In the adiabatic expansion phase, L roughly plateaus at a level set by the core entropy profile. That is, L during this phase is parametrized by $\psi_{c,i}$ and P_{orb} . Variations in the s profiles due to $M_{2,i}$

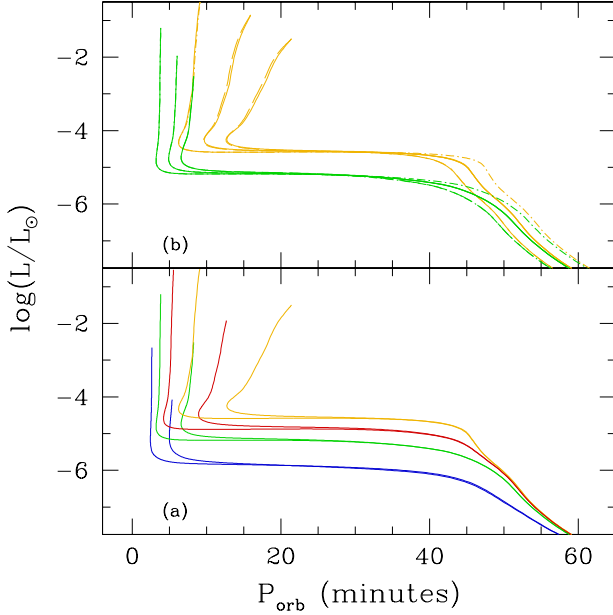


Figure 9. The dependence of the donor’s L -evolution on initial binary parameters. The line styles and colours have the same meanings as in Fig. 8. As in that figure, panel (a) shows the effects of varying $M_{2,i}$ and $\psi_{c,i}$ at fixed M_{tot} , while panel (b) examines the effects of varying M_{tot} , $M_{2,i}$ at fixed $\psi_{c,i}$. Here $M_{2,i}$ has values of 0.15, and 0.3 M_{\odot} . Evolution proceeds downward along each track and $M_{2,i}$ can be inferred from the initial P_{orb} within each set of constant $\psi_{c,i}$ tracks, with $M_{2,i}$ decreasing with increasing $P_{\text{orb},i}$.

differences are reflected in slight differences between tracks sharing $\psi_{c,i}$. During this phase, $L \approx 10^{-6} - 10^{-4} L_{\odot}$, while T_{eff} also plateaus at values $\approx 1000 - 1800$ K. The slow evolution in L ends once donor cooling sets in, producing the rapid decline starting between $P_{\text{orb}} \approx 40 - 50$ minutes. Panel (b) shows that a larger M_{tot} extends the P_{orb} at which donor cooling start (via an increased \dot{M}); M_{tot} thus parametrizes the L evolution during the cooling phase and beyond, with higher M_{tot} producing higher L at fixed P_{orb} .

The differences in $R_2(M_2)$ evolution with M_{tot} and $\psi_{c,i}$ are reflected in the binary’s $\dot{M}(P_{\text{orb}})$ evolution as shown in Fig. 10. For clarity, the evolution is shown for only four systems; these systems do, however, show the range of phase-space covered by the overall population in this study. We show models with $\log(\psi_{c,i}) = 3.0$ and 1.1, the latter providing a reasonable lower limit to the degeneracy expected in this population.

Although not shown by this plot, the $\dot{M}-P_{\text{orb}}$ evolution during turn-on is determined primarily by $M_{2,i}$ and $\psi_{c,i}$; M_{tot} influences only the \dot{M} maximum at large $\psi_{c,i}$. Once the systems have evolved into the expansion phase, the $P_{\text{orb}}-\dot{M}$ evolution depends only on M_{tot} and $\psi_{c,i}$, since donors with the same $\psi_{c,i}$ eventually follow the same $R_2(M_2)$ evolution. For GW-driven \dot{J} , at fixed P_{orb} , $\dot{M} \propto M_1^{2/3} M_2^2$ (for $M_2 \ll M_1$) so that the variations in the donors’ R_2 evolution produce a larger change in \dot{M} than do M_{tot} variations. This trend is shown in Fig. 10, where the family of curves with $\log(\psi_{c,i}) = 1.1$ lie significantly above those with $\log(\psi_{c,i}) = 3.0$. Within each set of curves at fixed $\psi_{c,i}$,

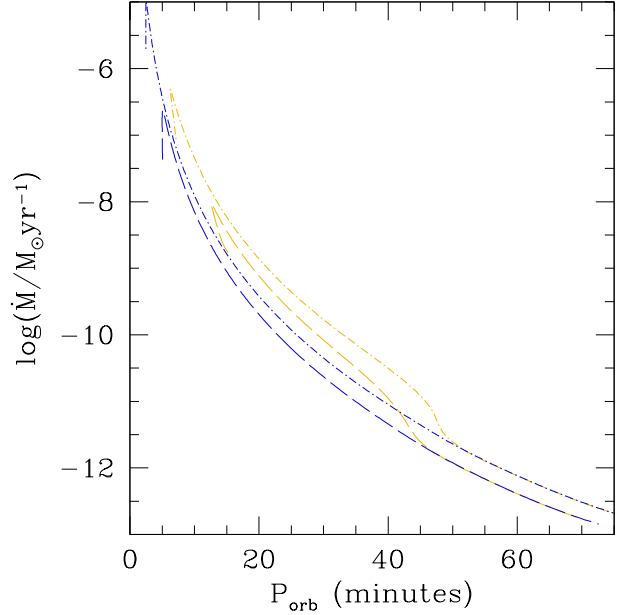


Figure 10. The dependence of the $\dot{M}-P_{\text{orb}}$ relation on initial binary parameters. The line styles and colours have the same meanings as in Fig. 8. For clarity, we display the evolution of two $(M_{1,i}, M_{2,i})$ pairs: (0.350, 0.150), and (1.025, 0.300), where values are in M_{\odot} and values of $\log(\psi_{c,i})$ of 3.0 and 1.1. The figure focuses on the \dot{M} evolution post \dot{M} -maximum. Evolution is first upward along the vertical sections of each track, then outward in P_{orb} as \dot{M} decreases. The range of \dot{M} at fixed P_{orb} displayed here represents the range available to WD channel AM CVn binaries given our assumptions in determining the donor’s initial entropy.

the spread in \dot{M} is caused by M_{tot} differences. Once donor cooling sets in, all tracks collapse toward the fully degenerate ones. Systems with lower $\psi_{c,i}$ and larger M_{tot} reach the fully degenerate tracks at longer P_{orb} . After this point, the $\dot{M}-P_{\text{orb}}$ relation is parametrized exclusively by M_{tot} .

4.3 Evolution with Irradiative Feedback

4.3.1 Comparison of the Irradiative and Donor’s Intrinsic Fluxes

The donor’s thermal evolution does not occur in isolation, but in the radiation bath provided by the flux from the accretor and disk. As the compressional heating luminosity generated in the accretor is always much less than the accretion luminosity (Bildsten et al. 2006), the external flux seen by the donor is dominated by the accretion light. To determine how important this external flux may be to the donor’s evolution, we calculate the accretion luminosity, L_{acc} , using

$$L_{\text{acc}} = \dot{M}(\phi_{L1} - \phi_{R1}), \quad (23)$$

where ϕ_{L1} , ϕ_{R1} are the gravitational potential at the inner Lagrange point and the accretor, respectively (Han & Webbink 1999), and then compare $T_{\text{irr}} = (L_{\text{acc}}/4\pi\sigma a^2)^{1/4}$ to the donor’s T_{eff} . We use equations (14)-(16) of Han & Webbink (1999) to calculate ϕ_{L1} , ϕ_{R1} (noting these authors interchange our definitions of M_1 and M_2).

The evolution of $T_{\text{eff}}/T_{\text{irr}}$ versus T_{eff} for the evolution tracks from Figure 10 is shown in Figure 11. During the

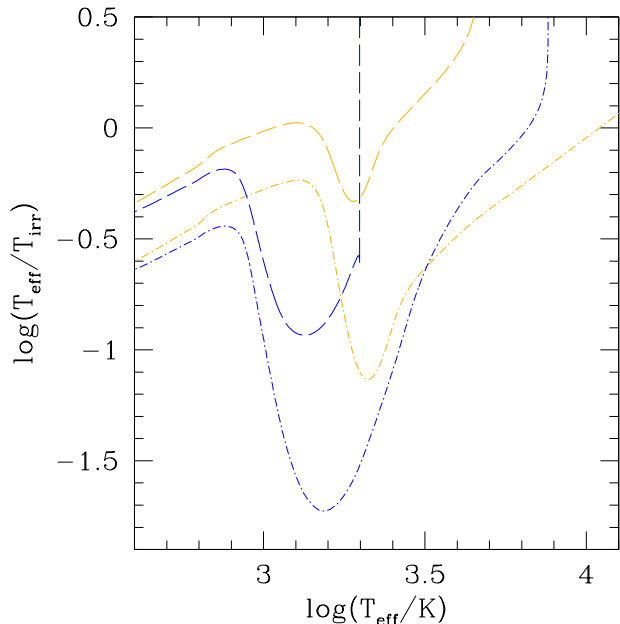


Figure 11. A comparison between the T_{eff} of non-irradiated donors and the T_{irr} produced by the system’s accretion flow. We show the same set of models as in Figure 10. Line styles and colours have the same meaning here as in that Figure. For the entire range of donors, irradiation dominates the donor’s outer boundary condition by the time \dot{M} has grown to its maximum value.

turn-on phase, T_{irr} increases rapidly, and by \dot{M} -maximum, T_{irr} has grown larger than T_{eff} by a up to a factor of 50. In all but the lowest M_{tot} and $\psi_{c,i}$ cases, T_{irr} remains greater than T_{eff} after this point. In most cases, T_{irr} strongly dominates T_{eff} . We consider now how this fact impacts the donor’s and binary’s evolution.

4.3.2 Our Irradiation Modelling

The general effect of external irradiation is to increase the temperature of the donor’s atmosphere (Milne 1926), which will tend to lower L and slow its cooling (see, e.g., Burrows et al. 2003; Baraffe et al. 2003, in the context of irradiated planets). The amount of heating depends on many factors: the irradiating flux’s intensity, spectrum, anisotropy, and the opacity sources in the donor’s atmosphere that determine its albedo (see, e.g., Vaz & Nordlund 1985; Barman et al. 2001; Sudarsky et al. 2003; Barman et al. 2004; Burkert et al. 2005). The detailed modelling of all these effects involves a multidimensional, non-grey, radiation-hydrodynamics problem and is beyond the scope of this paper. Thus, to model irradiation’s impact, we continue to assume grey opacities and alter our temperature outer boundary matching condition to $T_e = T_{\text{phot}}$, where T_{phot} is defined by

$$T_{\text{phot}}^4 = T_{\text{eff}}^4 + \eta \frac{T_{\text{irr}}^4}{4} = \frac{1}{4\pi\sigma} \left(\frac{L}{R_2^2} + \eta \frac{L_{\text{acc}}}{4a^2} \right), \quad (24)$$

where we assume a point-source geometry for L_{acc} and complete redistribution of the irradiating flux around the donor’s surface (Ritter et al. 2000). We also define the quantity

$L_{\text{surf}} = 4\pi\sigma R_2^2 T_{\text{phot}}^4$, which gives the total (intrinsic plus thermalized irradiative) luminosity off the donor’s surface. The factor η is a dimensionless efficiency parameter giving the fraction of L_{acc} that is thermalized in the donor’s photosphere. Equation (24) makes it clear that η parametrizes (within a grey, 1D model) our *entire* ignorance associated with the above uncertainties (including uncertainties in the assumed geometry).

For our calculations, we choose a fixed $\eta \leq 1.0$ and calculate L_{acc} from the system’s *secular* \dot{M} . However, AM CVn binaries experience a phase in which instabilities in the He accretion disk produce cyclical variations in \dot{M}_1 (Tsugawa & Osaki 1997). While these outbursts produce brightness variations $\lesssim 4$ magnitudes, the outburst period is ~ 5 days (Wood et al. 1987; Patterson et al. 1997, 2000). This corresponds roughly to a τ_{th} at $m' \lesssim 10^{-10} M_2$, so almost the entire donor is only aware of the time-averaged L_{acc} , making our use of the secular \dot{M} reasonable.

4.3.3 Impact of Irradiation on Donor & Binary Evolution

A star’s outer boundary condition only has a significant impact on its structure when the star is nearly fully convective (see, e.g., Kippenhahn & Weigert 1990, Sec. 10.3). Further, during the adiabatic phase of AM CVn evolution, mass loss, not thermal processes, dominate the donor’s evolution. Thus we can expect that irradiation will affect the donor’s evolution most during the cooling phase, by which time the donor’s are fully convective and thermal processes dominate their evolution. This expectation is borne out by our numerical calculations.

To illustrate this, we show in Figure 12 a comparison of $T(P)$ profiles between an irradiated ($\eta = 0.5$, red lines) and non-irradiated ($\eta = 0.0$, blue lines) donor at several specified values of M_2 along respective binary evolution calculations. Apart from the η differences, the initial conditions for the two calculations are the same. The profiles for $M_2 = 0.1999$ (solid lines), 0.1998 (short-dashed) and 0.1904 M_{\odot} (dashed) all occur during the turn-on and adiabatic phase. By $M_2 = 0.015 M_{\odot}$ (short-dash dotted line), the non-irradiated donor is in its cooling phase.

Throughout, T_{irr} dominates T_{phot} , so that the $\eta = 0.5$ donor’s T_{phot} -evolution tracks that of \dot{M} . By increasing T_{phot} , a constant T_{irr} will tend to reduce L (Baraffe et al. 2003; Burrows et al. 2003; Arras & Bildsten 2006). Here, there is at least one other effect important to the L evolution. Irradiated envelopes tend to have more extensive radiative regions and steeper entropy profiles. During rapid mass loss, this increases the L decrement a mass element experiences as it is advected outward.

Both effects contribute to lowering the donor’s L in the irradiated model. During phases of rapid mass loss, the latter effect even leads to a net $L < 0$ (most obviously seen in the inverted $T(P)$ profile of the $M_2 = 0.1904 M_{\odot}$ case, but also present at $M_2 = 0.1998 M_{\odot}$). A net $L < 0$ is produced when the flux cost required to advect material up the steep entropy gradient cannot be provided by donor’s intrinsic flux; the deficit is made up by absorption of irradiating flux and an inverted $T(P)$ profile results. Although some of the irradiating energy is absorbed below the photosphere, never more than $10^{-6} M_2$ of the donor is involved and the inward directed flux is always $\lesssim 0.01\eta\sigma T_{\text{irr}}^4$. The persistence

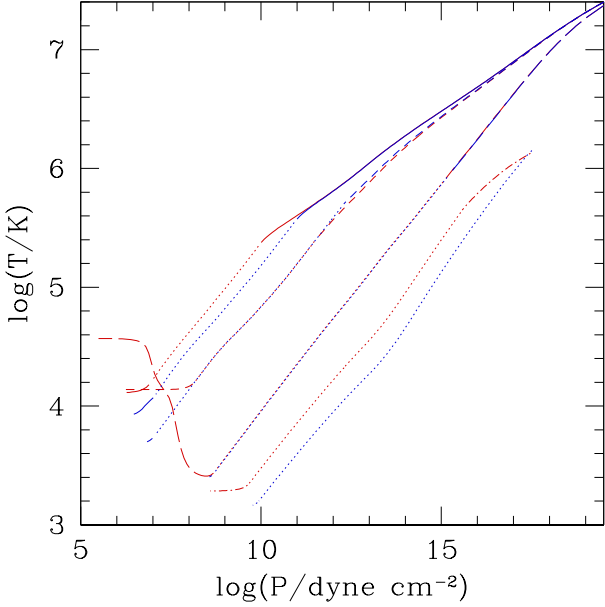


Figure 12. The $T(P)$ profiles for an $\eta = 0.5$ irradiated (red lines) and non-irradiated (blue lines) donor at points in their evolution when $M_2 = 0.1999$ (solid lines), 0.1998 (short-dashed), 0.1904 (dashed), and $0.015M_\odot$ (short-dash dotted); dotted portions of the lines indicate convective regions. The initial conditions for both sets of calculations were $M_{2,i} = 0.2$, $M_{1,i} = 0.625M_\odot$, and $R_{2,i} = 0.0380R_\odot$. Only once the non-irradiated donor is mainly convective and has begun its cooling phase ($M_2 = 0.015M_\odot$) do significant interior structural differences with the irradiated model appear.

of the $L < 0$ condition depends on \dot{M} and η , with L recovering to positive values once \dot{M} decreases sufficiently. For the case shown in Fig 12, $L < 0$ until $M_2 \approx 0.02M_\odot$, beyond the point the non-irradiated donor started its cooling phase.

Figure 12 further illustrates our general results that differences between the deep interior structures of irradiated and non-irradiated donors only extend as far as the base of the convective layer, roughly speaking. Thus it is only once the donors become nearly fully convective do significant structural differences occur; such differences become even more apparent once the non-irradiated donor begins its cooling (e.g., the $M_2 = 0.015M_\odot$ profiles in Fig. 12).

By decreasing L , the net effect of irradiation is to extend the adiabatic phase of evolution to lower M_2 and to slow the donor's cooling afterwards. Irradiated donors continue expanding to longer P_{orb} and contract more slowly once cooling begins. This alters the \dot{M} evolution, as illustrated in Figure 13. The solid lines show systems' evolution with non-irradiated donors, the short-dash dotted and dashed lines show $\eta = 0.1$ and $\eta = 0.5$ tracks, respectively. It can be seen that differences in \dot{M} evolution between η values appear even before the cooling phase for non-irradiated case. This reflects the outer boundary condition's growing importance in $\eta = 0.0$ donors, which have much deeper convective regions by this point in the evolution. As η is increased, the P_{orb} where the \dot{M} -decline occurs increases; this effect is more pronounced at lower $\psi_{c,i}$. Before contracting to the fully degenerate track, irradiated donors converge to an η -dependent, intermediate cooling track. In Fig. 13, this

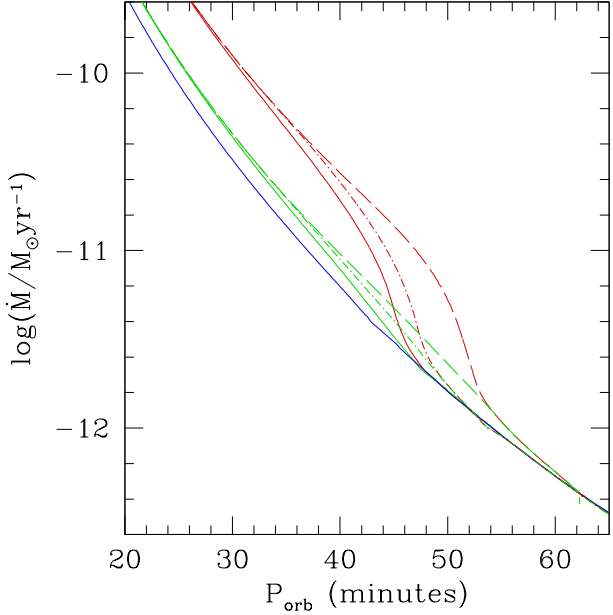


Figure 13. The impact of irradiation on the binary's \dot{M} evolution for the initial conditions $M_{2,i} = 0.2$ and $M_{1,i} = 0.625M_\odot$. Line colour indicates $\log(\psi_{c,i})$: 1.1 (red), 2.0 (green), and 3.0 (blue); line style indicates η : 0.0 (solid), 0.1 (short-dash dotted), and 0.5 (dashed). Only the non-irradiated $\log(\psi_{c,i}) = 3.0$ case is shown due to numerical difficulties in converging the irradiated models during the turn-on phase. However, from other irradiated models with $\log(\psi_{c,i}) = 3.0$ the irradiated $\log(\psi_{c,i}) = 3.0$ tracks will not differ substantially from the $\eta = 0.0$ track shown. For lower $\psi_{c,i}$, irradiation extends the adiabatic phase and slows the donor's cooling, elevating \dot{M} during these phases.

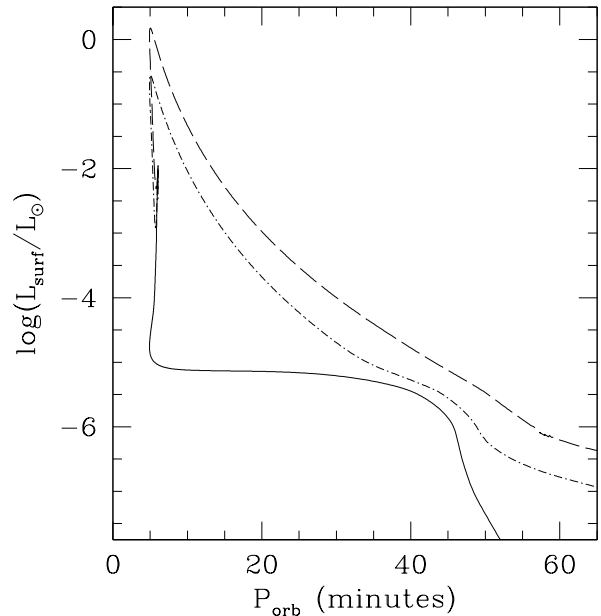


Figure 14. Irradiation's impact on the donor's L_{surf} in the limit of zero Bond albedo for systems sharing the initial conditions of $M_{2,i} = 0.2$, $M_{1,i} = 0.3M_\odot$, and $\log(\psi_{c,i}) = 2.0$. Line style has the same meaning as in Figure 13. In the $\eta \neq 0$ cases, irradiation substantially elevates L_{surf} .

occurs at $P_{\text{orb}} \approx 49(54)$ minutes for the $\eta = 0.1(0.5)$ tracks. By this point, the irradiated donors are fully convective, so that R_2 depends on s_c , M_2 , and the strength of irradiation (Arras & Bildsten 2006). As irradiation is a function of $M_2(R_2)$ through \dot{M} , the evolution of fully-convective donors within our model are parametrized exclusively by M_{tot} and η , as evidenced by this intermediate convergence.

The evolution of L_{surf} for a set of donors with differing η at fixed $M_{1,i}$, $M_{2,i}$, and $\psi_{c,i}$ are shown in Figure 14. Within our grey-atmosphere modelling, Fig. 14 can be interpreted as providing the donor’s surface luminosity in the limit of zero Bond Albedo. Since T_{irr} dominates T_{phot} over most of the evolution, the L_{surf} evolution mirrors that of \dot{M} . During the turn-on phase, L_{surf} decreases initially in all donors. This decrease is reversed for $\eta \neq 0$ by the \dot{M} growth. By \dot{M} maximum, $L_{\text{surf}} \approx 10^3 - 10^5$ higher in irradiated models compared to non-irradiated donors. During the adiabatic phase, L_{surf} decreases with \dot{M} , while the non-irradiated donor’s L plateaus. In the cooling phase L_{surf} converges towards tracks parametrized by η , but along much shallower slopes than non-irradiated donors. Even so, by $P_{\text{orb}} \approx 60$ minutes, even $\eta = 0.5$ donors are still rather dim, with $L_{\text{surf}} \lesssim 10^{-6} L_{\odot}$.

5 DISCUSSION AND APPLICATIONS

5.1 Comparison to Prior AM CVn Donor Models

We start our discussion by comparing the $\dot{M}(P_{\text{orb}})$ evolution produced in our current donor models to that produced by several prior donor models in Figure 15. The lower panel focuses on the comparison between our current models (solid lines) and the Deloye & Bildsten (2003) isentropic models (dashed lines). The Deloye & Bildsten (2003) models assume the donors are fully convective and application of these models in both Deloye & Bildsten (2003) and Deloye et al. (2005) also assume adiabatic donor evolution. Our more complete, current modelling shows that these He donors are not fully convective over much of the AM CVn evolution phase and that adiabatic evolution only occurs out to $P_{\text{orb}} \approx 40 - 55$ minutes.

The impact of these differences is apparent between the \dot{M} evolution shown by the dashed and solid lines in Fig. 15. The initial conditions (i.e. M_1 , M_2 , R_2) for each dashed line evolution equals the set of these values along the corresponding solid line at the point of intersection. From there, the isentropic donors produce \dot{M} evolution that increasingly diverges upwards from the solid-line tracks, even during the adiabatic evolution phase. This results from the realistic models being radiative throughout much of their core. Thus, compared to isentropic donors, the realistic models have a greater $\xi_{R_2} < 0$, even during adiabatic evolution (§4.1.1 and Appendix A). The differences between these evolution tracks become even more dramatic once the realistic donors begin cooling. Thus, modelling ultracompact binary evolution using isentropic donors will overestimate the R_2 expansion rate, the $\dot{M}-P_{\text{orb}}$ relations, and $P_{\text{orb}}(t)$.

This has implications for how \dot{M} measurements constrain an AM CVn system’s formation channel. Deloye et al. (2005) showed that assuming isentropic donors leads to a significant overlap in the $\dot{M}-P_{\text{orb}}$ plane between hot WD channel systems and He-star channel systems. The overlap

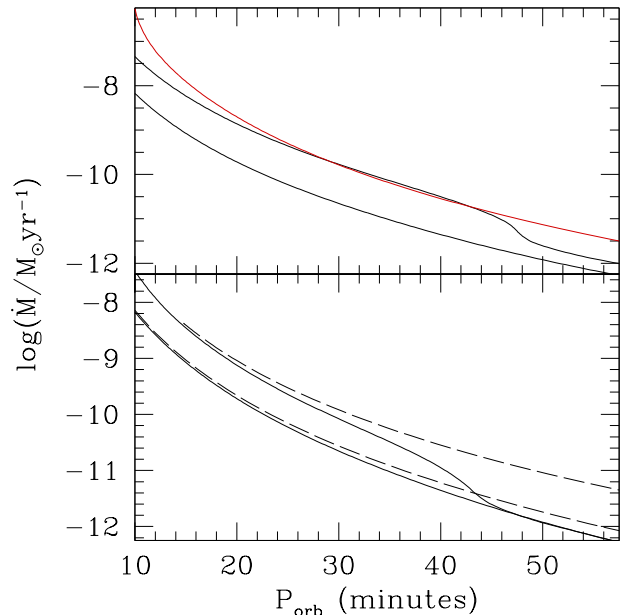


Figure 15. Comparison of AM CVn system’s outward $\dot{M}-P_{\text{orb}}$ evolution produced by different donor models. The lower panel compares evolution with our current models (solid lines) to that with the Deloye & Bildsten (2003) isentropic models (dashed lines). The two solid lines had $M_{2,i} = 0.2M_{\odot}$ and $\log(\psi_{c,i}) = 1.1$ (upper) and 3.5 (lower); in all four systems $M_{\text{tot}} = 0.5M_{\odot}$. The initial conditions (M_1 , M_2 , R_2) for each dashed line evolution equalled the set of these values on the corresponding solid line at the point of intersection. The upper panel compares evolution with our current models (solid lines, lower same as in lower panel, upper with $M_{\text{tot}} = 1.325$, $M_{2,i} = 0.3M_{\odot}$, $\log(\psi_{c,i}) = 1.1$) with the evolution produced by the semi-degenerate donor $M-R$ relation of Nelemans et al. (2001) with $M_{1,i} = 0.4$ and $M_{2,i} = 0.3M_{\odot}$ (red line).

between these channels is much reduced by with our current donor models, as illustrated in the upper panel of Fig. 15. There the black lines show the maximum range in the $\dot{M}-P_{\text{orb}}$ relation for WD channel AM CVn systems produced with our current unirradiated models. The red line shows the Nelemans et al. (2001) fit to a semi-degenerate donor $M(R)$ evolution with $M_{\text{tot}} = 0.7M_{\odot}$, and provides a rough lower limit to He-star channel systems’ $\dot{M}(P_{\text{orb}})$ evolution. Only the most massive WD channel systems have any overlap with He-star channel systems. Thus, given this current theory, a determination of a secular \dot{M} significantly above the upper black Fig. 15 would indicate a system formed through the He-star channel. This statement has one caveat: if WD channel systems have a maximum entropy greater than indicated by our determinations in §3 or if the donors are heated significantly (e.g., by tidal mechanisms) earlier in the AM CVn phase, then the overlap with the He-star channel systems could be increased.

We point out that modelling He-star channel systems with Nelemans et al. (2001) semi-degenerate $M(R)$ relation beyond $P_{\text{orb}} \gtrsim 45$ is problematic. This is because these donors will also begin cooling and contracting by these P_{orb} , similar to the WD channel donors. Thus, in reality, the red line in Fig 15 should begin a down turn somewhere in the vicinity of the $M_{\text{tot}} = 1.325M_{\odot}$ track. In fact, the original

calculation used by Nelemans et al. (2001) to determine this fit (model 1.1 of Tutukov & Fedorova 1989, see their Fig. 2) shows the start of this down turn at $P_{\text{orb}} \approx 40$ minutes. Thus, beyond the P_{orb} at which donors begin their cooling, \dot{M} measurements alone will not distinguish between formation channels.

5.2 The Orbital Period Distribution of WD-Channel AM CVn Binaries

While the changes to the adiabatic phase $M_2(R_2)$ evolution will quantitatively alter our expectations for the AM CVn population's P_{orb} -distribution, the detailed evolution to P_{orb} -minimum and the occurrence of donor cooling will produce qualitatively new features in the population's P_{orb} -distribution. We discuss these features here.

A key factor in how an individual system contributes to the P_{orb} -distribution is the time-derivative, \dot{P}_{orb} , of its P_{orb} -evolution. In a steady-state, continuity requires that the number density of systems at some P_{orb} , $n_{P_{\text{orb}}}$, scale as $n_{P_{\text{orb}}} \propto |1/\dot{P}_{\text{orb}}|$ (see, e.g., Deloye & Bildsten 2003). Here we will use this scaling relation to display steady-state distributions of systems sharing initial data. This provides a straightforward means for displaying how differing initial conditions influence the relative contribution systems make to the overall P_{orb} -distribution. We calculate \dot{P}_{orb} along an evolutionary track via

$$\frac{\dot{P}_{\text{orb}}}{P_{\text{orb}}} = 3 \left[\left(\frac{\dot{J}}{J} \right)_{\text{GW}} - \frac{\dot{M}_2}{M_2} (1 - q) \right]. \quad (25)$$

We show the evolution of \dot{P}_{orb} about the P_{orb} -minimum for a representative set of systems in Figure 16. These systems have $M_{1,i} = 0.575$, $M_{2,i} = 0.25M_{\odot}$, with colours indicating different $\psi_{c,i}$. The short-dash dotted segments indicate $\dot{P}_{\text{orb}} < 0$, solid segments $\dot{P}_{\text{orb}} > 0$. The black line shows the inward evolution due only to the $(\dot{J}/J)_{\text{GW}}$ term in equation (25) for comparison. As discussed in §4.1.1, the evolution here is most sensitive to $M_{2,i}$ and $\psi_{c,i}$. The \dot{P}_{orb} evolution reflects this, with $\psi_{c,i}$ (as illustrated in this figure) and $M_{2,i}$ both affecting the the value of the P_{orb} minimum and how \dot{P}_{orb} diverges from the GW-only evolution once contact occurs. The generic features of our this \dot{P}_{orb} evolution are the strong spikes at P_{orb} -minimum as \dot{P}_{orb} evolves through zero and the existence of \dot{P}_{orb} minimum and maximum that occur before and after P_{orb} -minimum, respectively.

The relative magnitude of \dot{P}_{orb} before and after the P_{orb} -minimum—which determines the relative number of systems evolving inward vs. outward in a steady-state—depends on $M_{2,i}$ and $\psi_{c,i}$. The $\dot{P}_{\text{orb}} < 0$ just before \dot{P}_{orb} -minimum is approximated by the GW-only rate, which scales as $(\dot{J}/J)_{\text{GW}}$. By \dot{P}_{orb} -maximum, \dot{M} has achieved its secular rate:

$$\left(\frac{\dot{M}_2}{M_2} \right)_{\text{eq}} = \frac{(\dot{J}/J)_{\text{GW}}}{5/6 + \xi_{R_2}/2 - q}, \quad (26)$$

producing a \dot{P}_{orb} during expansion:

$$\left(\frac{\dot{P}_{\text{orb}}}{P_{\text{orb}}} \right)_{\text{eq}} = 3 \left(\frac{\dot{J}}{J} \right)_{\text{GW}} \left[\frac{\xi_{R_2} - 1/3}{\xi_{R_2} + 5/3 - 2q} \right] \equiv 3 \left(\frac{\dot{J}}{J} \right)_{\text{GW}} \beta_{\dot{P}}. \quad (27)$$

If M_2 does not change appreciably from \dot{P}_{orb} -minimum to \dot{P}_{orb} -maximum, the term in square brackets, denoted here

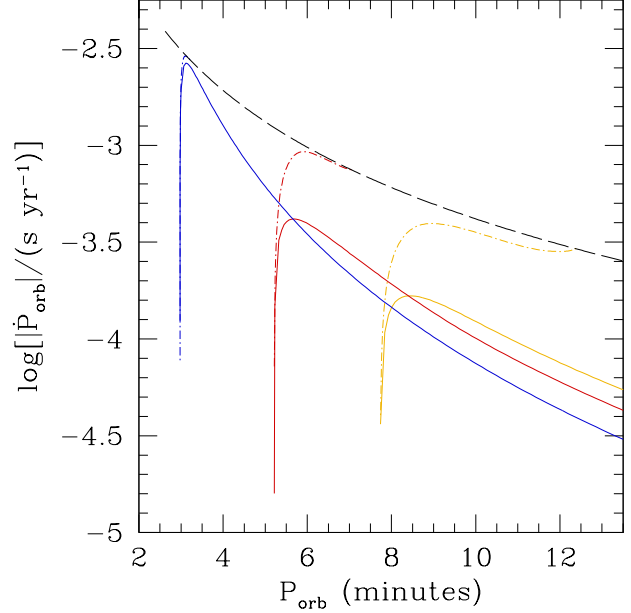


Figure 16. The evolution of \dot{P}_{orb} about the P_{orb} -minimum for representative systems with $M_{2,i} = 0.25$ and $M_{1,i} = 0.575M_{\odot}$. Line colour indicates $\log(\psi_{c,i})$: 1.1 (yellow), 1.5 (red), and 3.0 (blue). Short-dash dotted line segments indicate $\dot{P} < 0$, solid lines indicate $\dot{P} > 0$. The black line shows the corresponding inward \dot{P}_{orb} evolution produced by GW emission alone.

by $\beta_{\dot{P}}$, estimates the relative magnitudes of \dot{P}_{orb} before and after P_{orb} -minimum. Note that $\beta_{\dot{P}}$ depends on $\psi_{c,i}$ through ξ_{R_2} . During the early expansion phase, ξ_{R_2} evolves from 0 to ≈ -0.3 to -0.05 . With $0 \leq q \leq 2/3$ (the q range considered here), $\beta_{\dot{P}}$ can vary considerably. Typically, $-1 < \beta_{\dot{P}} < 0$, as seen in Fig. 16. However, for larger q and $\psi_{c,i}$, $\beta_{\dot{P}}$ can be much less than -1; we see this behaviour in our calculations with $M_{1,i} = 0.3$, $M_{2,i} = 0.2M_{\odot}$ for $\log(\psi_{c,i}) \geq 3.0$. Lower $\psi_{c,i}$ donors have smaller relative outward-to-inward $|\dot{P}_{\text{orb}}|$, for two reasons. One, lower $\psi_{c,i}$ leads to larger minimum ξ_{R_2} , producing slower expansion and $\beta_{\dot{P}}$ values closer to zero. Two, M_2 during the \dot{P}_{orb} -transition is not fixed, with M_2 losses greater for lower $\psi_{c,i}$. This results in a lower \dot{J} loss rate post \dot{P}_{orb} -maximum, further contributing to smaller $\dot{P}_{\text{orb}} > 0$.

How the evolution near P_{orb} -minimum translates into the steady-state P_{orb} -distributions is shown in Figure 17. There we display histograms of relative system numbers along evolutionary tracks with $M_{1,i} = 0.575$, $M_{2,i} = 0.25$. The number in each bin, N , is calculated by integrating $n_{P_{\text{orb}}} dP_{\text{orb}}$ over each bin. The overall normalization is arbitrary but fixed across tracks, so that the histograms accurately reflect relative \dot{P}_{orb} rates. The lower panel displays separately the contributions from the $\dot{P}_{\text{orb}} < 0$ (short-dash dotted lines) and $\dot{P}_{\text{orb}} > 0$ (solid lines) segments of the evolution. The black line in the lower-panel shows the corresponding result for a GW-only driven in-spiral. The upper panel shows the sum of contributions from both inward and outward evolving systems.

The general trends in the lower panel are the slight deviation from GW-only evolution from contact inward, followed by a peak as $\dot{P}_{\text{orb}} \rightarrow 0$ at P_{orb} -minimum. The out-

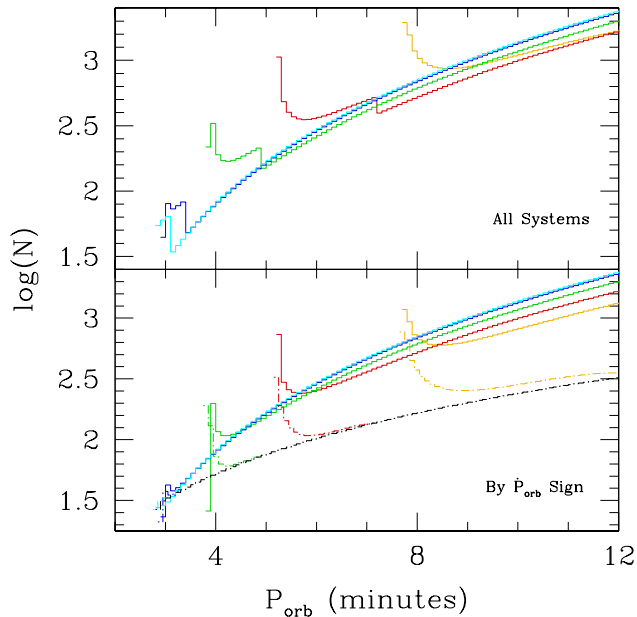


Figure 17. Histograms of relative numbers of AM CVn systems in a steady-state along single evolution tracks. All tracks have $M_{1,i} = 0.575$ and $M_{2,i} = 0.25M_{\odot}$ with colour indicating $\log(\psi_{c,i})$: 1.1 (yellow), 1.5 (red), 2.0 (green), 3.0 (blue), and 3.5 (cyan). The lower panel separates systems by \dot{P}_{orb} sign: the short-dash dotted histograms counts inward moving systems, the solid histograms outward moving systems. The upper panel displays the sum of both inward and outward moving systems. The black short-dash dotted line shows the evolution produced by GW emission alone (i.e. $\dot{M} = 0$). The bins have width of $\Delta P_{\text{orb}} = 6$ s. The overall normalization is arbitrary, but the relative normalization accurately reflects the relative \dot{P}_{orb} rates.

wardly evolving systems likewise show peaks just post P_{orb} -minimum. For larger P_{orb} , lower- $\psi_{c,i}$ tracks lead to fewer systems at a given P_{orb} since hotter donors have larger M_2 , producing larger $(\dot{J}/J)_{\text{GW}}$ (Deloye et al. 2005, see also Fig. 16). The sharp steps in the upper-panel histograms result from starting our calculations at the point of contact (i.e. pre-contact evolution is not included), so the location and size of each step is somewhat artificial. However, since they result from having a definite starting point for the GW-driven in-spiral, as is provided by the CE-event forming these systems, there is a physical basis for expecting their existence.

The most striking feature of these histograms are the strong peaks at each system’s P_{orb} -minimum. The impact of these features on the integrated AM CVn P_{orb} -distribution below $P_{\text{orb}} \approx 15$ minutes will depend on the distribution of initial conditions, the survival of systems at contact (see, e.g., Marsh et al. 2004), and how He-star channel systems contribute in this P_{orb} range. Determining how the integrated P_{orb} -distribution depends on initial conditions and the physics determining the outcomes at contact is the subject of current work. This will be most relevant to future space-based GW-interferometers, such as *LISA*, which will provide a rather complete census of the galactic AM CVn population at these P_{orb} (Nelemans et al. 2001) and offer direct observational tests of these predictions.

In Deloye & Taam (2006), we considered the relevance of the $\dot{P}_{\text{orb}} < 0$ phase to the short period X-ray variables, RX J0806+1527 (321 s; Beuermann et al. 1999) and RX J1914+2456 (569 s; Haberl & Motch 1995). There is still some question as to the nature of these two sources (see discussion in Deloye & Taam 2006, and references therein). If both system’s periods are orbital and their measured \dot{P}_{orb} (Strohmayer 2004, 2005) secular, then Deloye & Taam (2006) showed that both are consistent with being members of the AM CVn population. If this is the case, there is the question of whether observing either system in its present state is an extremely unlikely event.

A detailed answer to this question is beyond the scope of this paper. However, a related question can be posed: what is the relative likelihood of detecting each system in its $\dot{P}_{\text{orb}} < 0$ versus $\dot{P}_{\text{orb}} > 0$ phase? Figure 18 provides a partial answer. The lower panel shows the \dot{P}_{orb} evolution for two sets of AM CVn systems, each of which bracket the evolution of systems consistent with either RX J0806+1527 or RX J1914+2456 (see Deloye & Taam 2006). The upper panel shows, for these evolution tracks, the ratio of the number of systems with $\dot{P}_{\text{orb}} > 0$ to those with $\dot{P}_{\text{orb}} < 0$ in steady-state. This ratio is only $\approx 1.3 - 2.3$ for periods below each system’s measure P_{orb} . Thus, there is not a strong a priori bias to detecting such systems in their $\dot{P}_{\text{orb}} > 0$ phase, although the actual relative detection likelihood between the two phases is likely influenced strongly by selection effects.

We now turn to how donor cooling influences the P_{orb} -distribution. By the time \dot{P}_{orb} has passed its maximum, it is evolving at a rate given by equation (27), and is essentially determined by \dot{M} (which is a function of M_{tot} and $\psi_{c,i}$). This is seen in the lower panel of Figure 19 where we display \dot{P}_{orb} versus P_{orb} for two different M_{tot} at two different $\psi_{c,i}$. Before systems begin their cooling phase, the ordering of tracks is for lower $\psi_{c,i}$ donors to produce higher \dot{P}_{orb} . After the cooling phase ends, tracks are distinguished only by M_{tot} . During cooling, the donor’s contraction stalls the P_{orb} evolution, producing a reversal in the ordering of \dot{P}_{orb} with $\psi_{c,i}$ and a distinctive peak in the steady-state P_{orb} distribution along each track (upper panel of Fig. 19).

The location and magnitude of these peaks are determined by M_{tot} and $\psi_{c,i}$. The system’s M_{tot} determines the P_{orb} at which cooling becomes important, with larger M_{tot} moving the peak’s centre to longer P_{orb} . The donor’s $\psi_{c,i}$ determines the degree of donor contraction; hotter donors lead to slower \dot{P}_{orb} during the cooling phase and larger peaks. In slowing donor cooling, irradiation also acts to shift the peak centres to longer P_{orb} . The distribution of AM CVns above $P_{\text{orb}} \approx 40$ minutes will provide an integrated diagnostic of the distribution of $\psi_{c,i}$, M_{tot} , and η . In this P_{orb} range, AM CVn binaries will not be individually resolvable GW-sources due to the galactic foreground of detached WD-WD binaries (Nelemans et al. 2001). Thus, whether the system distribution in this P_{orb} range can be a practical diagnostic tool must await observations progress in the optical/IR wave bands.

5.3 The Eclipsing AM CVn SDSS J0926+3624: Evidence for Non-Zero Entropy Donors from the WD Channel

Although we reserve detailed applications of the models presented here to specific AM CVn systems for a later compan-

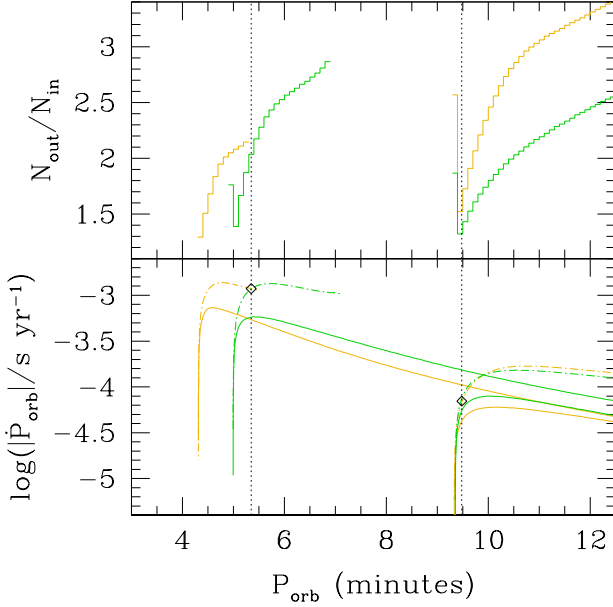


Figure 18. The evolution rates for AM CVn system models consistent with measured properties of RX J0806+1527 (lines at $P_{\text{orb}} \approx 5$ minutes) and RX J1914+2456 (lines at $P_{\text{orb}} \approx 9$ minutes). The set of two lines shown for each system indicates the approximate range of variation allowed by observations and our modelling. Different colours are meant only to guide the eye in matching tracks within and between the two panels. The lower panel shows the \dot{P}_{orb} evolution for the selected tracks, with solid lines indicating $\dot{P}_{\text{orb}} > 0$ and short-dash dotted lines $\dot{P}_{\text{orb}} < 0$. The upper panel shows the ratio of number of systems with $\dot{P}_{\text{orb}} > 0$ to those with $\dot{P}_{\text{orb}} < 0$ assuming steady-state. The dotted lines indicates the measured P_{orb} of each system, while the diamonds show their measured \dot{P}_{orb} . In making these comparisons, we explicitly assume the measured \dot{P}_{orb} reflects the system’s *secular* \dot{P}_{orb} .

ion paper, we shall discuss the recently discovered eclipsing AM CVn binary, SDSS J0926+3624 (Anderson et al. 2005) as a system for which the entropy of the donor can be probed. This is especially important as the distribution of donor entropy provides (i) a potential diagnostic of AM CVn formation channels and (ii) constrains the stellar binary evolution determining AM CVn initial conditions (Deloye et al. 2005). Bildsten et al. (2006) have presented evidence based on accretor properties that the two known long-period AM CVn binaries, GP Com ($P_{\text{orb}} = 46.6$ minutes) and CE-315 ($P_{\text{orb}} = 65.1$ minutes) both harbour a relatively hot donor. Additionally, if early-contact AM CVn binaries are indeed the correct model for the systems RX J0806+1527 and RX J1914+2456, then this would provide further evidence for hot donors: the bracketing models shown in Fig. 18, have a range of $\log(\psi_{c,i}) \approx 1.3 - 1.8$ for RX J0806+1527 and $\approx 1.2 - 1.5$ for RX J1914+2456. SDSS J0926+3624, however, has finally provided direct evidence for hot donors in AM CVn binaries.

This evidence comes in the form of M_1 and M_2 determinations made via modelling of eclipse light-curves (Marsh et al. 2006). Assuming the accretor obeys a fully degenerate WD M - R relation (a good approximation at the determined M_1), these authors determine $M_1 = 0.84 \pm 0.05 M_{\odot}$

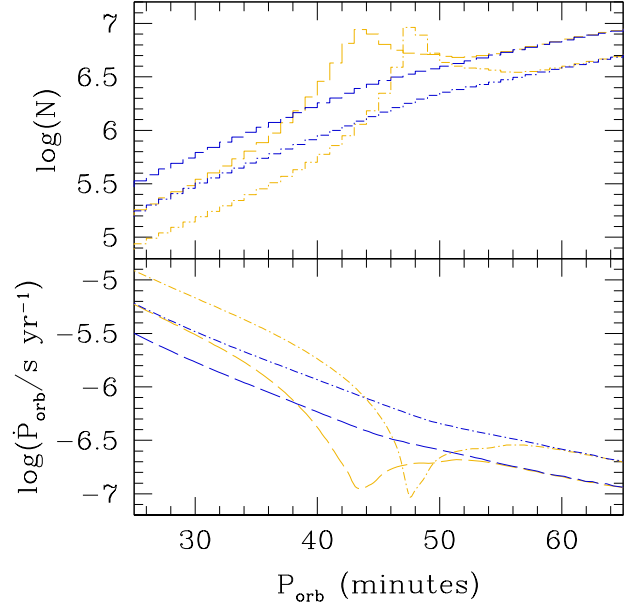


Figure 19. The evolution of \dot{P}_{orb} for $P_{\text{orb}} > 25$ min during the expansion phase. The lower panel shows \dot{P}_{orb} vs. P_{orb} for two sets of M_{tot} each with two different $\log(\psi_{c,i})$. Colours indicate $\log(\psi_{c,i})$ and have the same meaning as in Fig. 17. Dashed lines show systems with $M_{1,i} = 0.35$, $M_{2,i} = 0.15 M_{\odot}$; short-dash dotted lines systems with $M_{1,i} = 1.025$, $M_{2,i} = 0.3 M_{\odot}$. The upper panel shows the relative number of systems expected in steady-state along each evolution track. As in Fig. 17, the overall normalization is arbitrary, but the relative normalization between tracks is set by their \dot{P}_{orb} rates. The slowing of \dot{P}_{orb} during the donor’s cooling phase leads to a peak in system numbers. The peak’s P_{orb} is diagnostic of M_{tot} (as well as η , although this is not show here). The magnitude of the peak increases with decreasing $\psi_{c,i}$.

and $q = 0.035 \pm 0.002$, giving $M_2 = 0.029 \pm 0.002 M_{\odot}$, $\approx 50\%$ more massive than a zero-temperature WD that fills its Roche lobe at this system’s $P_{\text{orb}} = 28.3$ minutes. This M_2 measurement provides us the first direct means of determining an AM CVn donor’s current entropy. From the determined M_2 -range, we find that $\log(\psi_{c,i})$ lies approximately in the range 1.60–1.35. If the actual range of He-star channel donor M - R evolution does not differ significantly from the Nelemans et al. (2001) fit for these systems, then a He-star channel system should have $M_2 \approx 0.05 M_{\odot}$ at $P_{\text{orb}} = 28.3$ minutes. The evolve-MS channel also appears to produce a value of M_2 which is too high for systems at this P_{orb} (see Table 1 of Podsiadlowski et al. 2003). Thus SDSS J0926+3624 presents evidence that the WD channel indeed contributes to the observed AM CVn population and that this channel produces non-zero entropy donors as predicted by Deloye et al. (2005).

We can also predict the current \dot{M} in SDSS J0926+3624. From our calculations, a system with the determined value of $M_{\text{tot}} = 0.869 M_{\odot}$ and $M_2 = 0.029 M_{\odot}$ at $P_{\text{orb}} = 28.3$ minutes, has an $\dot{M} = 9.8 \times 10^{-11} M_{\odot} \text{ yr}^{-1}$. At fixed P_{orb} when $M_2 \ll M_1$, $\dot{M} \propto M_1^{2/3} M_2^2 \propto M_1^{8/3} q^2$ (Deloye et al. 2005), so the error bars quoted in Marsh et al. (2006) for M_1 and q provide an error of $\approx 20\%$ on \dot{M} . Thus, we estimate $\dot{M} \approx 9.8 \times 10^{-11} \pm 2.0 \times 10^{-11} M_{\odot} \text{ yr}^{-1}$. This \dot{M} range is close to value at which the accretor’s thermal evolu-

tion decouples from the compressional heating provided by the accretion (Bildsten et al. 2006). Thus, we can use Fig. 1 from Bildsten et al. (2006) to estimate the accretor’s T_c from \dot{M} and find $T_c \approx 1.8\text{--}2.1 \times 10^7$ K. Using these \dot{M} and T_c ranges, we sum the accretor’s cooling and compressional luminosity (see §2 of Bildsten et al. 2006) to estimate the accretor’s $T_{\text{eff}} \approx 21,300\text{--}23,800$ K, taking $M_1 = 0.84M_\odot$ to determine $R_1 \approx 0.01R_\odot$. More refined estimates of the accretor’s thermal properties will require more detailed calculations taking into account variations in \dot{M} evolution histories, the time-dependent evolution of the accretor’s envelope during the decoupling phase, and possibly the effect of He shell flashes on the accretor’s surface.

The measurements of M_{tot} and $\psi_{c,i}$ in additional systems are required before the observational distributions of these parameters can be determined. However, the likelihood of discovering a system such as SDSS J0926+3624 given our theoretical models of the WD channel AM CVn population can be considered. We first compare M_{tot} to the distribution in Fig. 1 of Nelemans et al. (2001). The locus of points defining the region $M_{\text{tot}} = 0.869 \pm 0.05M_\odot$ in this figure lies outside the $M_1\text{--}M_2$ parameter space these authors consider most likely. This raises the question of whether observing such a high M_{tot} in SDSS J0926+3624 simply is the result of small number statistics or whether this is a hint of additional physics that skews the M_{tot} distribution to higher values. An example of such physics would be the preferential survival of high $M_{1,i}$ systems during a direct impact accretion phase at contact (Marsh et al. 2004). Finally, from Figure 3, about 12% of WD channel AM CVn systems in our modelling have $\psi_{c,i}$ in the range consistent with SDSS J0926+3624, not taking into account the system’s high M_{tot} . Given the rather flat $\psi_{c,i}$ distribution expected from theory, determining M_{tot} and ψ_c constraints in additional AM CVn systems is essential if we are to determine if this is consistent with our theoretical expectations or not.

5.4 Observational Signatures of AM CVn Donors

Here we consider predictions for the donor’s contribution to the system’s light in SDSS J0926+3624 based on our current models. The near edge-on inclination of SDSS J0926+3624 makes this system a good candidate for discriminating the accretor’s and donor’s light without significant contamination from the accretion disk. The discovery spectrum of SDSS J0926+3624 (Anderson et al. 2005) is reproduced in Figure 20 from the SDSS archival data. It was obtained over a 3600s exposure—roughly two system orbits—and thus provides a phase averaged spectrum. It is decidedly non-blackbody in shape, indicating that a DB WD accretor is not the only contributor to the system’s light.

The question is whether the second component contributing to the flux is the donor or the disk? The Marsh et al. (2006) M_1, M_2 constraints imply $R_1 \approx 0.01R_\odot$ and $R_2 = 0.043R_\odot$. From our current modelling, we predict the donor’s $T_{\text{eff}} \approx 1750\text{--}4500$ K, corresponding to an η range of 0.0–0.5. With $i = 83.1^\circ$ and $q = 0.035$ (Marsh et al. 2006), the projected area of the disk’s face $\approx 2.7R_2^2$; i.e., out of eclipse roughly equivalent areas of disk and donor surfaces are seen. Thus, the disk may provide a significant contribution to the system’s light. Indeed, Marsh et al. (2006) find that the disk contributes $\approx 50\%$ of the flux in the r' band

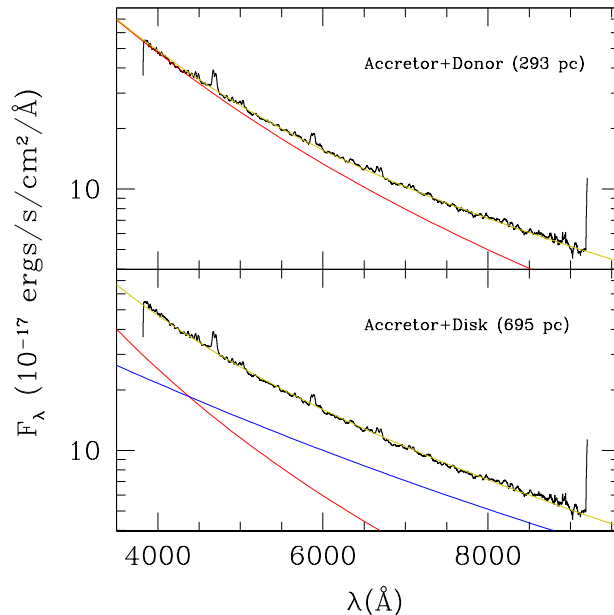


Figure 20. Comparison between the Sloan spectrum for SDSS J0926+3624 (black line) and theoretical models. The upper panel shows a model spectrum (yellow line) calculated using contributions from a $T_{\text{eff}} = 21,000$ K, $R_1 = 0.01R_\odot$ accretor (red line) and $T_{\text{eff}} = 4400$ K, $R_2 = 0.043R_\odot$ donor (which lies below the x-axis) at a distance of 293 pc. The lower panel shows the combined spectrum (yellow line) from a $T_{\text{eff}} = 39,000$ K accretor (red line) and a steady-state α -disk model (blue line) with $\dot{M} = 9.8 \times 10^{-11} M_\odot \text{ yr}^{-1}$ at a distance of 695 pc.

and $\approx 25\%$ in the g' . They also find significant inter-orbit variability, so whether this particular ratio of flux contributions is representative of conditions during the Sloan observation is not certain.

Given the prominent double-peaked He emission lines in this system, AM CVn phenomenology would argue the disk is either in a stable, seemingly optically thin, low-state or is an outbursting disk caught in quiescence. In either case, a stable, optically thick α -disk model spectra is not expected. To check this, we calculated an α -disk spectra assuming $\dot{M} = 9.8 \times 10^{-11} M_\odot \text{ yr}^{-1}$ and an outer radius of $0.7a$. We added this to the accretor’s flux modelled as a single T_{eff} blackbody. We then adjusted this T_{eff} and the system’s distance to give a “by eye” best fit to the SDSS J0926+3624 spectrum. The results are shown in the lower panel of Figure 20. A rather hot, $T_{\text{eff}} = 39,000$ K, accretor and a system distance of 695 pc is required for a reasonable fit. This model underestimates the continuum flux at wavelengths $\lambda \lesssim 4000$ Å and $\lambda \gtrsim 8000$ Å. Additionally, the r' flux from the disk is significantly greater than the accretor, in disagreement with Marsh et al. (2006). This however may not be a significant issue given the source’s variability.

We also considered a model with accretor and donor contributions, but no disk. Both components were modelled as single T_{eff} blackbodies. The observed spectra is well fit by the combination of a $T_{\text{eff}} = 21,000$ K accretor and a $T_{\text{eff}} = 4,400$ K donor at a distance of 293 pc (upper panel of Figure 20). The accretor’s T_{eff} is a little below the range predicted by the Bildsten et al. (2006) theory (§5.3), while

the donor's T_{eff} is consistent with an η somewhat below 0.5. The fit in this case is somewhat better than the accretor+disk model. We should note that other acceptable fits can be found by collectively increasing or decreasing both components' temperatures and the system's distance. Thus, higher accretor T_{eff} require higher η values for the donor to be hot enough to produce a good fit to the spectra.

A parallax measurement for SDSS J0926+3624 will clearly distinguish between the stable α -disk+accretor and the accretor+donor model (as well as further constrain the component temperatures in this latter model). The better agreement between data and donor+accretor model and our expectation that the disk is not in a stable high-state already argues for the donor+accretor model. Given our poor understanding of a low-state disk spectra and flux, however, one can only conclude that an accretor+donor model is fully consistent with both the observed spectrum and all theoretical expectations for SDSS J0926+3624. Since this model doesn't include any disk contributions, it does fail to explain the inferred disk properties of the Marsh et al. (2006) results. It may be possible that it is a cool disk providing the long- λ flux in this system, possibly explaining both the Sloan spectrum and the Marsh et al. (2006) results. Better understanding of quiescent He disks and phase-resolved spectral studies of this system may both be required to break this degeneracy between either a cold disk or donor as the source of long wavelength flux.

6 SUMMARY

We have implemented a new stellar evolution code in C++ that allows significant flexibility in use of input physics and defining systems of ODEs. This code has been used to model, for the first time, the full stellar structure of the donors in WD-channel AM CVn binaries. Specifically, the thermal and structural evolution of the donor has been calculated to determine how the donor's thermal evolution affects the evolution of the binary and to provide the first predictions for the donor's light in these systems.

Systems forming through the WD channel are expected to have a range of donor properties, most importantly a range of initial (i.e., at contact) degeneracy (Deloye et al. 2005). We modelled the pre-contact evolution of WD channel systems based on the Nelemans et al. (2001) population synthesis to determine suitable initial donor models for our subsequent calculations. The donors in this population have initial central degeneracy parameters between $\psi_{c,i} \approx 10$ - 10^4 , with the distribution in $\psi_{c,i}$ being rather flat between $\psi_{c,i} \approx 25$ -4000. Most of these systems make contact at $P_{\text{orb}} \approx 2$ -11 minutes. This range of donor parameters is likely dependent on assumptions about the binary evolution leading to their formation (in particular the CE-event prior to the AM CVn phase) and our assumptions about the donor's cooling during the pre-contact phase. Quantifying the potential effects of these assumptions will require more extensive modelling of the proto-donors in this pre-contact phase.

Our evolutionary calculations show that WD-channel AM CVn systems have three phases of evolution. An \dot{M} turn-on phase, during which \dot{M} grows to its maximum value while R_2 contracts under mass loss, and P_{orb} decreases. This

behaviour produces a turn-on phase lasting significantly longer than previous estimates (e.g., Marsh & Nelemans 2005; Willems & Kalogera 2005): $\sim 10^4$ - 10^6 yrs depending on the donor's initial $\psi_{c,i}$. In the second phase, the donor expands adiabatically under mass loss. The third phase begins once the mass loss rate and the donor's thermal time have both decreased enough to allow, starting at $P_{\text{orb}} \approx 45$ minutes, the donor to cool and contract to a fully degenerate configuration. We discussed how the system's initial conditions influence the later evolution of $R_2(M_2)$ and $\dot{M}(P_{\text{orb}})$. We also revised the upper limit to the $\dot{M} - P_{\text{orb}}$ relation for WD-channel systems (given our initial condition determinations). Finally, we predicted the donor's intrinsic L and T_{eff} ; during the adiabatic phase, $L \approx 10^{-6}$ - $10^{-4} L_{\odot}$, while $T_{\text{eff}} \approx 1000$ - 1800 K.

The flux generated by the accretion flow in these systems can easily dominate the donor's intrinsic thermal output. We self-consistently modelled the impact of the accretion light on the donor's and binary's evolution in the grey approximation. The irradiation reduces the donor's intrinsic L , producing a delay in the onset of cooling and slowing the donor's contraction once cooling does begin. This shifts the downturn in the $\dot{M}(P_{\text{orb}})$ relation seen in the non-irradiated donors to longer P_{orb} . Irradiation also elevates the donor's photospheric temperature and surface luminosity (up to 10,000 K and $10^{-2} L_{\odot}$, respectively, during the adiabatic phase). The observational signatures of irradiation depend on the irradiating flux's spectra, the opacity sources in the donors atmosphere and the efficiency of day-to-night side energy flow, all considerations beyond this work's scope. Our predictions for the irradiated donor's light are thus approximate and valid in the limit of complete redistribution of flux in a grey atmosphere with a Bond albedo of zero.

In comparison to prior predictions using simpler donor models, we find that previous assumptions of fully-convective donors and adiabatic evolution (Deloye & Bildsten 2003; Deloye et al. 2005) are not valid over much of the AM CVn evolution. The donors only become fully convective at $P_{\text{orb}} \approx 40$ minutes and $M_2 \approx 0.01$. Prior to this, their shallower entropy profile leads to a slower expansion rate relative to fully convective models. Due to this, we argue that prior to the onset of cooling, \dot{M} measurements could distinguish between systems formed in the He-star versus WD channels (as opposed to the conclusions of Deloye et al. 2005). After the cooling phase develops, all initial donor entropy information, including any that distinguishes formation channels, will be erased.

A system's evolution about its P_{orb} -minimum and the occurrence of donor cooling phase both leave diagnostic signatures on the AM CVn population's P_{orb} -distribution. Most significantly, the evolution of $\dot{P}_{\text{orb}} \rightarrow 0$ at the P_{orb} -minimum and the slowing of P_{orb} evolution that occurs during the cooling phase lead to peaks in the P_{orb} -distribution whose location and size depend on initial parameters (and η in the case of the cooling peaks). These could provide observational diagnostics of the distribution of these parameters in the galactic AM CVn population.

Finally, we showed that recent measurements of M_1 and M_2 in the eclipsing AM CVn system, SDSS J0926+3624 (Marsh et al. 2006) provide direct evidence that WD-channel systems contribute to the AM CVn population and that this channel produces non-zero entropy donors as pre-

dicted by Deloye et al. (2005). We compared predictions for this system's light based on our models, showing that a composite spectrum consisting of donor and accretor contributions is fully consistent with this system's discovery spectra. Based on this, we predict this system lies at a distance of ≈ 290 pc.

Current investigations include applying this theory to interpret the improving observational constraints in many of the known AM CVn systems (e.g., Roelofs et al. 2007, submitted). In addition, we are considering how the physics relevant to the AM CVn system formation and early contact-phase survival could be probed by future *LISA* observations of the P_{orb} -distribution of sources at $P_{\text{orb}} \lesssim 15$ minutes. Other indicated work includes proper non-grey, phase dependent modelling of the donor's irradiated atmosphere as well as progress on understanding the contribution of low-state He accretion disks to the system's emission.

ACKNOWLEDGMENTS

We thank the anonymous referee for a careful reading of this manuscript and for suggestions that improved its overall presentation. We thank Susana Barros, Gijs Roelofs, Tom Marsh, Gijs Nelemans, Bart Willems, and Dean Townsley for helpful discussions and encouragement during the preparation of this manuscript, as well as Jason Alexander for providing the low-temperature opacity tables needed in this work and for answering associated questions. For material support, CJD thanks Craig Heinke, Vicky Kalogera, and Greg and Lauree Hickok, without whose help this work could not have been completed. This work was supported by NASA through XMM grant NNX06AH62G and by the NSF through grants AST-0200876 and AST-0449558.

APPENDIX A: THE R_2 RESPONSE TO MASS LOSS

The donor's R_2 can be expressed as the integral of equation (3):

$$R_2^3 = \frac{3}{4\pi} \int_0^{M_2} \frac{dm}{\rho}. \quad (\text{A1})$$

The derivative of equation (A1) with respect to M_2 is

$$\begin{aligned} \frac{dR_2}{dM_2} &= \frac{1}{4\pi R^2} \left[\frac{1}{\rho_{\text{phot}}} - \int_0^{M_2} \frac{dm}{\rho} \left(\frac{d \ln \rho}{dM_2} \right)_m \right] \\ &= \frac{1}{4\pi R_2^2} \left[\frac{1}{\rho_{\text{phot}}} - \int_0^{M_2} \frac{dm}{\rho} \left(\frac{1 - \chi_T \nabla'}{\chi_\rho} \right) \left(\frac{d \ln P}{dM_2} \right)_m \right], \end{aligned} \quad (\text{A2})$$

where $\chi_\rho = (\partial \ln P / \partial \ln \rho)_T$, $\chi_T = (\partial \ln P / \partial \ln T)_\rho$ and $\nabla' = (\partial \ln T / \partial \ln P)_m$ gives the change in T at fixed m that occurs due to changes in M_2 .

The quantity $(d \ln P / dM_2)_m \sim d \ln P / dm \sim P_c / (PM_2)$, showing the donor's outer layers dominate the R_2 response to M_2 . Also, $(\partial \ln T / \partial \ln P)_m > 0$ and $\nabla' \leq \nabla_{\text{ad}}$ generically in our donors, so the local response to mass loss at fixed m is an expansion in r . The surface term then is the only driver of R decrease under mass loss (see also Hjelming 1989). Note that both these behaviours are apparent in Fig. 4.

How the R_2 evolution depends on the donor's structure

is more easily seen by transforming to P -coordinates and considering only the donor's outer layers. The contribution, δR_2 , to R_2 between surface at P_{phot} and some pressure $P_b \gg P_{\text{phot}}$:

$$\delta R_2 = \frac{1}{g_b} \int_{P_{\text{phot}}}^{P_b} \frac{dP}{\rho}. \quad (\text{A3})$$

where $g_b \approx \text{const.}$ is the gravitational acceleration at P_b . The change in this layer's thickness under mass loss is then:

$$\frac{d(\delta R_2)}{dM_2} = -\frac{1}{g_b} \int_{P_{\text{phot}}}^{P_b} \frac{dP}{\rho} \left(\frac{d \ln \rho}{dM_2} \right)_P, \quad (\text{A4})$$

where we have neglected for simplicity the surface term's contribution. The layer's response then depends on $(d \ln \rho / dM_2)_P$, which can be rewritten as

$$\begin{aligned} \left(\frac{d \ln \rho}{dM_2} \right)_P &= \left[- \left(\frac{\partial \ln \rho}{\partial \ln P} \right)_{M_2} + \left(\frac{\partial \ln \rho}{\partial \ln P} \right)_m \right] \left(\frac{d \ln P}{dM_2} \right)_m \\ &= \frac{\chi_T}{\chi_\rho} (\nabla - \nabla') \left(\frac{d \ln P}{dM_2} \right)_m. \end{aligned} \quad (\text{A5})$$

APPENDIX B: THE LUMINOSITY PROFILE'S RESPONSE TO MASS LOSS

To examine how the donor's l -profile evolution in response to mass loss depends on the donor's structure and relative ordering of τ_{th} and τ_{m} , taking $\epsilon = 0$ we can rewrite equation (4) as

$$\begin{aligned} \frac{d \ln l}{dm} &= -\frac{c_P T}{l} (\nabla' - \nabla_{\text{ad}}) \left(\frac{\partial \ln P}{\partial t} \right)_m \\ &\approx -\frac{c_P T}{l} (\nabla' - \nabla_{\text{ad}}) \left(\frac{\partial \ln P}{\partial M_2} \right)_m \dot{M}_2. \end{aligned} \quad (\text{B1})$$

where the first approximation holds when mass loss effects dominate $(\partial \ln P / \partial t)_m$ and the elapsed time under consideration $\delta t \ll \tau_{\text{th}}$. In the outer layers, the region most heavily weighted by the $d \ln P / dM_2$ term (see Appendix A), this last expression can be expressed approximately as

$$\frac{d \ln l}{dm} \approx \frac{\tau_{\text{th}}}{\tau_{\text{m}}} (\nabla' - \nabla_{\text{ad}}) \frac{\partial \ln P}{\partial M_2}. \quad (\text{B2})$$

Where $\delta t \ll \tau_{\text{th}} \ll \tau_{\text{m}}$, heat transport is able to approximately maintain the original thermal profile, producing $\nabla' \approx \nabla$. For radiative regions, $\nabla < \nabla_{\text{ad}}$, producing $d \ln l / dm < 0$ as mass elements must absorb flux in order to increase their entropy as they move outward. In convective regions, $d \ln l / dm \gtrsim 0$. Since the fractional change in l , $\delta l / l$ due to advection goes as $\sim \tau_{\text{th}} / \tau_{\text{m}}$, the overall flux decrement is rather small in this limit.

In the opposite limit, when $\tau_{\text{th}} \gg \tau_{\text{m}}$, mass elements are advected outward nearly adiabatically. Thus $\nabla' \rightarrow \nabla_{\text{ad}}$ from below in radiative regions and from above in convective zones. Since $\tau_{\text{th}} / \tau_{\text{m}}$ can become very large, significant l perturbations due to mass loss can be driven by only a very slight non-adiabaticity in the advective flow. Our numerical calculations bear this out, showing that the magnitude of l perturbations are largest during the adiabatic mass loss phases.

REFERENCES

- Anderson S. F., et al., 2005, *AJ*, 130, 2230
- Arras P., Bildsten L., 2006, *ApJ*, 650, 394
- Baraffe I., Chabrier G., Barman T. S., Allard F., Hauschildt P. H., 2003, *A&A*, 402, 701
- Barman T. S., Hauschildt P. H., Allard F., 2001, *ApJ*, 556, 885
- Barman T. S., Hauschildt P. H., Allard F., 2004, *ApJ*, 614, 338
- Beuermann K., Thomas H.-C., Reinsch K., Schwobe A. D., Trümper J., Voges W., 1999, *A&A*, 347, 47
- Bildsten L., Townsley D. M., Deloye C. J., Nelemans G., 2006, *ApJ*, 640, 466
- Büning A., Ritter H., 2006, *A&A*, 445, 647
- Burkert A., Lin D. N. C., Bodenheimer P. H., Jones C. A., Yorke H. W., 2005, *ApJ*, 618, 512
- Burrows A., Sudarsky D., Hubbard W. B., 2003, *ApJ*, 594, 545
- Chabrier G., Baraffe I., 1997, *A&A*, 327, 1039
- Deloye C. J., Bildsten L., 2003, *ApJ*, 598, 1217
- Deloye C. J., Bildsten L., Nelemans G., 2005, *ApJ*, 624, 934
- Deloye C. J., Taam R. E., 2006, *ApJ*, 649, L99
- Eggleton P. P., 1971, *MNRAS*, 151, 351
- Farmer A. J., Phinney E. S., 2003, *MNRAS*, 346, 1197
- Faulkner J., 1976, in Eggleton P., Mitton S., Whelan J., eds, *Structure and Evolution of Close Binary Systems* Vol. 73 of IAU Symposium, Gravitational Radiation and the Evolution of Low Mass Binaries. pp 193–+
- Ferguson J. W., Alexander D. R., Allard F., Barman T., Bodnarik J. G., Hauschildt P. H., Heffner-Wong A., Tamanai A., 2005, *ApJ*, 623, 585
- Girardi L., Bressan A., Bertelli G., Chiosi C., 2000, *A&AS*, 141, 371
- Haberl F., Motch C., 1995, *A&A*, 297, L37+
- Han Z., Webbink R. F., 1999, *A&A*, 349, L17
- Hjellming M. S., 1989, PhD thesis, University of Illinois at Urbana-Champaign
- Iglesias C. A., Rogers F. J., 1996, *ApJ*, 464, 943
- Kippenhahn R., Weigert A., 1990, *Stellar Structure and Evolution*. Springer-Verlag Berlin Heidelberg New York.
- Kolb U., Baraffe I., 1999, *MNRAS*, 309, 1034
- Kolb U., Ritter H., 1990, *A&A*, 236, 385
- Landau L. D., Lifshitz E. M., 1971, *The classical theory of fields*. Oxford: Pergamon Press, 1971, 3rd rev. engl. edition
- Marsh T. R., Dhillon V. S., Littlefair S., Groot P., Hakala P., Nelemans G., Ramsay G., Roelofs G., Steeghs D., 2006, To appear in Proc 15th European White Dwarf Workshop (astro-ph/0610414)
- Marsh T. R., Nelemans G., 2005, *MNRAS*, 363, 581
- Marsh T. R., Nelemans G., Steeghs D., 2004, *MNRAS*, 350, 113
- Milne E. A., 1926, *MNRAS*, 87, 43
- Nelemans G., Portegies Zwart S. F., Verbunt F., Yungelson L. R., 2001, *A&A*, 368, 939
- Nelemans G., Yungelson L. R., Portegies Zwart S. F., 2001, *A&A*, 375, 890
- Paczyński B., 1967, *Acta Astronomica*, 17, 287
- Paczynski B., 1976, in Eggleton P., Mitton S., Whelan J., eds, *IAU Symp. 73: Structure and Evolution of Close Binary Systems Common Envelope Binaries*. pp 75–+
- Patterson J., Kemp J., Shambrook A., Thomas E., Halpern J. P., Skillmand D. R., Harvey D. A., Vanmunster T., Retter A., Fried R., Buckley D., Nogami D., Kato T., Baba H., 1997, *PASP*, 109, 1100
- Patterson J., Walker S., Kemp J., O’Donoghue D., Bos M., Stubbings R., 2000, *PASP*, 112, 625
- Paxton B., 2004, *PASP*, 116, 699
- Podsiadlowski P., Han Z., Rappaport S., 2003, *MNRAS*, 340, 1214
- Potekhin A. Y., Baiko D. A., Haensel P., Yakovlev D. G., 1999, *A&A*, 346, 345
- Press W. H., Teukolsky S. A., Vetterling W. T., Flannery B. P., 1992, *Numerical recipes in C. The art of scientific computing*. Cambridge: University Press, —c1992, 2nd ed.
- Ritter H., 1988, *A&A*, 202, 93
- Ritter H., Zhang Z.-Y., Kolb U., 2000, *A&A*, 360, 969
- Schaller G., Schaerer D., Meynet G., Maeder A., 1992, *A&AS*, 96, 269
- Strohmayer T. E., 2004, *ApJ*, 610, 416
- Strohmayer T. E., 2005, *ApJ*, 627, 920
- Sudarsky D., Burrows A., Hubeny I., 2003, *ApJ*, 588, 1121
- Taam R. E., Sandquist E. L., 2000, *ARA&A*, 38, 113
- Tsugawa M., Osaki Y., 1997, *PASJ*, 49, 75
- Tutukov A. V., Fedorova A. V., 1989, *Soviet Astronomy*, 33, 606
- Vaz L. P. R., Nordlund A., 1985, *A&A*, 147, 281
- Webbink R. F., 1984, *ApJ*, 277, 355
- Willems B., Kalogera V., 2005, *ArXiv Astrophysics e-prints*, astro-ph/0508218
- Winisdoerffer C., Chabrier G., 2005, *Phys. Rev. E*, 71, 026402
- Wood M. A., Winget D. E., Nather R. E., Hessman F. V., Liebert J., Kurtz D. W., Wesemael F., Wegner G., 1987, *ApJ*, 313, 757